





















Toward a Galactic Distribution of Planets. I. Methodology and Planet Sensitivities of the 2015 High-cadence *Spitzer* Microlens Sample

Wei Zhu (祝伟)^{1,16,17} , A. Udalski^{2,18}, S. Calchi Novati^{3,4,16} , S.-J. Chung^{5,6,17} , Y. K. Jung^{7,17} , Y.-H. Ryu^{5,17} ,
I.-G. Shin^{7,17}, A. Gould^{1,5,8,16,17}, C.-U. Lee^{5,6,17}, M. D. Albrow^{9,17} , J. C. Yee^{7,16,17} , C. Han¹⁰ , K.-H. Hwang⁵ ,
S.-M. Cha^{5,11}, D.-J. Kim⁵ , H.-W. Kim⁵, S.-L. Kim^{5,6}, Y.-H. Kim⁵, Y. Lee^{5,11}, B.-G. Park^{5,6}, R. W. Pogge¹ 

(KMTNet Collaboration),

R. Poleski^{1,2}, P. Mróz², P. Pietrukowicz² , J. Skowron² , M. K. Szymański², S. Kozłowski² , K. Ulaczyk^{2,12}, M. Pawlak²
(OGLE Collaboration),

and

C. Beichman¹³, G. Bryden¹⁴, S. Carey¹⁵ , M. Fausnaugh¹, B. S. Gaudi¹ , C. B. Henderson^{14,19} , Y. Shvartzvald^{14,19} , and
B. Wibking¹
(Spitzer Team)

¹ Department of Astronomy, Ohio State University, 140 W. 18th Ave., Columbus, OH 43210, USA; zhu.908@osu.edu

² Warsaw University Observatory, Al. Ujazdowskie 4, 00-478 Warszawa, Poland

³ IPAC, Mail Code 100-22, Caltech, 1200 E. California Blvd., Pasadena, CA 91125, USA

⁴ Dipartimento di Fisica “E. R. Caianiello,” Università di Salerno, Cia Giovanni Paolo II, I-84084 Fisciano (SA), Italy

⁵ Korea Astronomy and Space Science Institute, 776 Daedeokdae-ro, Yuseong-Gu, Daejeon 34055, Korea

⁶ Korea University of Science and Technology, 217 Gajeong-ro, Yuseong-gu, Daejeon 34113, Korea

⁷ Harvard-Smithsonian Center for Astrophysics, 60 Garden St., Cambridge, MA 02138, USA

⁸ Max-Planck-Institute for Astronomy, Königstuhl 17, D-69117 Heidelberg, Germany

⁹ Department of Physics and Astronomy, University of Canterbury, Private Bag 4800 Christchurch, New Zealand

¹⁰ Department of Physics, Chungbuk National University, Cheongju 361-763, Korea

¹¹ School of Space Research, Kyung Hee University, Giheung-gu, Yongin, Gyeonggi-do, 17104, Korea

¹² Department of Physics, University of Warwick, Gibbet Hill Road, Coventry, CV4 7AL, UK

¹³ NASA Exoplanet Science Institute, MS 100-22, California Institute of Technology, Pasadena, CA 91125, USA

¹⁴ Jet Propulsion Laboratory, California Institute of Technology, 4800 Oak Grove Dr., Pasadena, CA 91109, USA

¹⁵ Spitzer Science Center, MS 220-6, California Institute of Technology, Pasadena, CA 91125, USA

Received 2017 January 5; revised 2017 September 19; accepted 2017 September 19; published 2017 November 6

Abstract

We analyze an ensemble of microlensing events from the 2015 *Spitzer* microlensing campaign, all of which were densely monitored by ground-based high-cadence survey teams. The simultaneous observations from *Spitzer* and the ground yield measurements of the microlensing parallax vector π_E , from which compact constraints on the microlens properties are derived, including $\lesssim 25\%$ uncertainties on the lens mass and distance. With the current sample, we demonstrate that the majority of microlenses are indeed in the mass range of M dwarfs. The planet sensitivities of all 41 events in the sample are calculated, from which we provide constraints on the planet distribution function. In particular, assuming a planet distribution function that is uniform in $\log q$, where q is the planet-to-star mass ratio, we find a 95% upper limit on the fraction of stars that host typical microlensing planets of 49%, which is consistent with previous studies. Based on this planet-free sample, we develop the methodology to statistically study the Galactic distribution of planets using microlensing parallax measurements. Under the assumption that the planet distributions are the same in the bulge as in the disk, we predict that $\sim 1/3$ of all planet detections from the microlensing campaigns with *Spitzer* should be in the bulge. This prediction will be tested with a much larger sample, and deviations from it can be used to constrain the abundance of planets in the bulge relative to the disk.

Key words: gravitational lensing: micro – methods: statistical – planetary systems – planets and satellites: dynamical evolution and stability

Supporting material: data behind figures, machine-readable tables

1. Introduction

The distribution of planets in different environments is of great interest. Studies have shown that the planet frequency may be correlated with the host star metallicity (e.g., Santos et al. 2001, 2003; Fischer & Valenti 2005; Wang & Fischer

2015; Zhu et al. 2016b), the stellar mass (e.g., Johnson et al. 2010), stellar multiplicity (e.g., Eggenberger et al. 2007; Wang et al. 2014), and exterior stellar environment (e.g., Thompson 2013). For this purpose, probing the planet distribution outside the solar neighborhood is important. In particular, the planet distribution in the Galactic bulge, given its unique environment, can provide an extra dimension to test and further develop our theories of planet formation.

Probing the distribution of planets in the Galactic bulge, or, more generally, at all Galactic scales, is a unique application of

¹⁶ Spitzer Team.

¹⁷ KMTNet Collaboration.

¹⁸ OGLE Collaboration.

¹⁹ NASA Postdoctoral Program Fellow.

Galactic microlensing because of its independence from the flux from the planet host (Mao & Paczynski 1991; Gould & Loeb 1992). For example, Penny et al. (2016) used an ensemble of 31 microlensing planets and found tentative evidence that the bulge might be deficient of planets compared to the disk.

While microlensing is in principle sensitive to planets at various Galactic distances, the distance determination of any given microlensing event is nontrivial. This is because, in the majority of cases, the only relevant observable from the microlensing light curve is the Einstein timescale

$$t_E \equiv \frac{\theta_E}{\mu_{\text{rel}}}. \quad (1)$$

Here μ_{rel} is lens–source relative proper motion, and θ_E is the angular Einstein radius,

$$\theta_E \equiv \sqrt{\kappa M_L \pi_{\text{rel}}}; \quad \kappa \equiv \frac{4G}{c^2 \text{au}} \simeq 8.14 \frac{\text{mas}}{M_\odot}, \quad (2)$$

where M_L is the lens mass, $\pi_{\text{rel}} \equiv \text{au}(D_L^{-1} - D_S^{-1})$ is the lens–source relative parallax, and D_L and D_S are distances to the lens and the source (i.e., the star being lensed), respectively. In planetary events, θ_E is usually also measurable through the so-called finite-source effect (Yoo et al. 2004), in addition to two parameters that characterize the planet itself: the planet/star mass ratio q and the planet/star separation s in units of θ_E (Gaudi & Gould 1997b). There nevertheless remains a degeneracy between the lens mass and lens distance (assuming that the source is in the bulge, which is almost always the case). The difficulty in precisely determining the lens distance is a significant weakness of ground-based microlensing in determining the Galactic distribution of planets, as has been demonstrated by Penny et al. (2016).

The most efficient way to determine or better constrain the lens distance D_L is by measuring the so-called microlens parallax vector π_E ,

$$\pi_E \equiv \frac{\pi_{\text{rel}} \mu_{\text{rel}}}{\theta_E \mu_{\text{rel}}}, \quad (3)$$

which can be effectively achieved by simultaneously observing the same event from at least two well-separated ($\mathcal{O}(1 \text{ au})$) observatories (Refsdal 1966; Gould 1994). This is because, for typical Galactic microlensing events, the projected Einstein radius on the observer plane,

$$\tilde{r}_E = \frac{\text{au}}{\pi_E}, \quad (4)$$

is of order $\sim 10 \text{ au}$, and thus observers separated by $\sim 1 \text{ au}$ would see considerably different light curves of the same microlensing event. For events with θ_E measurements, including most planetary events, most binary events, and relatively rare single-lens events, the measurements of π_E directly yield the lens mass and lens–source relative parallax

$$M_L = \frac{\theta_E}{\kappa \pi_E}; \quad \pi_{\text{rel}} = \theta_E \pi_E, \quad (5)$$

the latter being a good proxy for distinguishing disk and bulge lenses (see Section 4). For the great majority of single-lens events, θ_E cannot be measured from the microlensing light

curve, but the lens distribution (M_L and π_{rel}) can be much more tightly constrained once π_E is measured, as first pointed out by Han & Gould (1995).

For this reason, the *Spitzer Space Telescope* has been employed for microlensing (Dong et al. 2007; Gould et al. 2013, 2014, 2015a, 2015b, 2016). The 2014 *Spitzer* microlensing experiment served as a pilot program that successfully demonstrated the ability to measure microlens parallax using *Spitzer* (Calchi Novati et al. 2015; Udalski et al. 2015b; Yee et al. 2015a; Zhu et al. 2015a). Starting in 2015, the main goal of *Spitzer* microlensing campaigns became measuring the Galactic distribution of planets (Calchi Novati et al. 2015; Yee et al. 2015b).

It is by no means trivial to organize *Spitzer* and ground-based observations to enable a measurement of the Galactic distribution of planets that is unbiased by observational decisions. On the one hand, microlensing events must be chosen for *Spitzer* observations very carefully in order to maximize both the sensitivity to planets of the whole sample and the probability that these observations will actually lead to a microlens parallax measurement. On the other hand, these observational decisions cannot in any way be influenced by whether planets have (or have not) been detected. The first objective requires that observational decisions make maximal use of available information, while the second means that a certain “blindness” to this information must be rigorously enforced. Yee et al. (2015b) discussed in great detail how to optimize observations while enforcing this blindness, and a short summary is given in Section 2.3. Interested readers are urged to consult Yee et al. (2015b) for more details.

Following the Yee et al. (2015b) protocol, the 2015 *Spitzer* microlensing campaign observed 170 microlensing events that were first found in the ground-based microlensing surveys, namely, the Optical Gravitational Lensing Experiment (OGLE; Udalski 2003; Udalski et al. 2015a) and the Microlensing Observations in Astrophysics (MOA; Bond et al. 2001; Sako et al. 2008). In this work, we present analysis of 50 of them that fall within the footprints of OGLE and the prime fields of the newly established KMTNet (Korean Microlensing Telescope Network; Kim et al. 2016).

The present work is not aimed at directly answering how planets are distributed within the Galaxy. Instead, we develop a framework within which the above question can be ultimately addressed. It is nevertheless true that the 50 events in our sample, observed at a ~ 10 -minute cadence nearly continuously throughout the year 2015, are more sensitive to planets than the majority of the remaining events in the 2015 *Spitzer* sample. Another significant contributor to the overall planet sensitivity would be high-magnification events, which have nearly 100% sensitivity to planets (Griest & Safizadeh 1998; Gould et al. 2010) but are considerably rarer. These high-magnification events will be analyzed separately.

This paper is organized as follows. Section 2 summarizes our observations and reduction methods for both ground-based and space-based data. Section 3 describes our selection of the raw sample. In Section 4 we provide the methodology for analyzing individual events, including fourfold solutions, distance and mass estimations, and planet sensitivity computation. This method is then applied to the current sample, and results are presented in Section 5. In Section 6 we discuss the implications of this work, as well as outline the path for future work.

Table 1
Summary of the 50 Events in Our Sample

OGLE #	R.A. (deg)	Decl. (deg)	l (deg)	b (deg)	Subjective Selection	Objective Selection	OGLE-IV Fields, Cadences (per day)	<i>Spitzer</i> Observations Start, Stop, #
0011	269.217833	-29.283250	0.957550	-2.289872	5-30-11:59	...	BLG505, 30	7184.96, 7222.58, 53
0029	269.944167	-28.644944	1.828415	-2.522683	5-10-14:33	6-01	BLG505, 30	7185.31, 7222.89, 52
0034	270.580333	-27.516083	3.088357	-2.452817	4-28-17:01	6-08	BLG511, 10	7186.01, 7222.92, 62
0081	268.653000	-28.996278	0.957513	-1.719135	6-01-14:25	...	BLG505, 30	7184.10, 7221.81, 57
0350	268.248583	-31.820278	-1.657210	-2.846465	5-19-20:45	6-01	BLG535, 3	7183.95, 7221.76, 61
0379	269.104292	-29.574056	0.656089	-2.350021	5-19-20:45	6-01	BLG505, 30	7184.61, 7222.58, 54
0388	268.468917	-28.534028	1.274824	-1.346174	5-10-14:33	6-01	BLG500, 10	7183.98, 7221.81, 66
0461	270.043208	-28.156944	2.295828	-2.356385	5-19-20:45	...	BLG504, 10	7185.79, 7222.90, 58
0529	270.264667	-29.922917	0.854524	-3.397576	5-16-22:18	6-08	BLG513, 3	7185.79, 7222.92, 51
0565	269.153708	-29.128056	1.063892	-2.163672	5-16-22:18	6-01	BLG505, 30	7184.62, 7222.59, 53

Note. Here (R.A., decl.) are the equatorial coordinates, and (l , b) are the galactic coordinates. We also include the subjective selection dates and objective selection dates (if objective criteria are met), OGLE-IV bulge fields, and cadences. In the last column, we present the HJD dates of the first and last *Spitzer* observation, as well as the total number of observations from *Spitzer*.

(This table is available in its entirety in machine-readable form.)

2. Observations and Data Reductions

2.1. OGLE

All events in our sample were found by the Optical Gravitational Lensing Experiment (OGLE) collaboration in real time through its Early Warning System (Udalski et al. 1994; Udalski 2003), based on observations with the 1.4 deg² camera on its 1.3 m Warsaw Telescope at the Las Campanas Observatory in Chile (Udalski 2003; Udalski et al. 2015a). These events received OGLE-IV observations with cadences varying from 3 to 30 per day. The coordinates, OGLE-IV fields, and cadences of individual events are provided in Table 1.

OGLE data were reduced using the photometry software developed by Wozniak (2000) and Udalski (2003), which was based on the Difference Image Analysis (DIA) technique (Alard & Lupton 1998).

2.2. KMTNet

KMTNet consists of three 1.6 m telescopes located at CTIO in Chile, SAAO in South Africa, and SSO in Australia. Observations were initiated on February 3 (JD = 2,457,056.9), February 19 (JD = 2,457,072.6), and June 9 (JD = 2,457,182.9) in 2015 from CTIO, SAAO, and SSO, respectively. Each telescope is equipped with a 4 deg² field-of-view camera and observes the ~16 deg² prime microlensing fields at a ~10-minute cadence when the bulge is visible.

The KMTNet data were reduced by the DIA photometric pipeline (Alard & Lupton 1998; Albrow et al. 2009).

2.3. *Spitzer*

As detailed in Yee et al. (2015b), the *Spitzer* program is designed to maximize the sum of the products $\sum_i S_i P_i$, where S_i is the planet sensitivity of event i and P_i is the probability to measure the microlens parallax of this event. As a consequence, the *Spitzer* team started selecting targets beginning in early 2015 May, although *Spitzer* did not start taking data until JD' = JD - 2,450,000 = 7180.2 (2015 June 6.7). To enforce our blindness to the existence of planets in any events, we select events if (1) they meet certain objective criteria at the time of one of the uploads of targets to *Spitzer*, in which case they are considered as “objectively chosen,” or (2) they do not meet objective criteria but are nevertheless selected on the basis

that the *Spitzer* team believes that by selecting them the quantity $\sum_i S_i P_i$ can be maximized. Events selected in the latter case are known as “subjectively chosen.” For objectively chosen events, planets and planet sensitivities from before or after the *Spitzer* selection dates can be incorporated into the statistical analysis, while for subjectively chosen events, only planets (and planet sensitivities) from after the *Spitzer* selection dates can be included in the final sample.²⁰ One relevant point is that any event that is originally subjectively chosen but later meets objective criteria will be considered as objectively chosen (provided that its parallax is measurable based on the restricted set of *Spitzer* data acquired after the date it became objective).

Events, once selected, are given *Spitzer* cadences according to suggestions in Yee et al. (2015b). The majority of events received *Spitzer* observations at a 1-day cadence. Higher cadences were assigned to a few events, if the *Spitzer* team believed that the nominal cadence would lead to failures in parallax measurements. After all targets were scheduled according to their adopted cadences, the remaining time, if any, was applied to events that appeared or would appear with relatively high magnification as seen from the ground. *Spitzer* observations stopped if the predefined criteria for stopping observations in Yee et al. (2015b) were met, or the event exited the *Spitzer* Sun-angle window. Our last *Spitzer* observation was taken on JD' = 7222.28. In Table 1 we provide the information for *Spitzer* selection and observation of each individual event.

Spitzer data were reduced using the customized software that was developed by Calchi Novati et al. (2015) specifically for this program. This software improved the performance of *Spitzer* IRAC photometry in crowded fields, although unknown systematics may persist in some cases. We discuss this in Section 5.1.

2.4. Additional Color Data

The characterization of a microlensing event requires a measurement of the color of the source star. This is usually achieved by using the less frequent V-band observations from survey teams, but it does not work for events that are highly

²⁰ More precisely, planets (and the putative planets needed for the sensitivity calculation) that are detectable in data that were available to the team prior to their decision must be excluded.

extincted in optical bands. For this reason, we also obtained observations of all *Spitzer* targets using the ANDICAM (DePoy et al. 2003) dichroic camera on the 1.3 m SMARTS telescope at CTIO. These observations were made simultaneously in *I* and *H* bands and were for the specific purpose of inferring the $I - [3.6\mu\text{m}]$ color of the source star. These additional color data were reduced using DoPhot (Schechter et al. 1993).

3. Raw Sample Selection

According to Yee et al. (2015b), only events in which π_E can be “measured” are useful for the study of the Galactic distribution of planets. While the phrase “ π_E is measured” is not defined until Section 5.2, we provide here our procedure for raw sample selection.

In 2015, there are in total 68 *Spitzer* events that fall within the footprints of KMTNet prime fields. The following events are excluded from the raw sample for various reasons:

1. Three were not covered by OGLE; they were selected for *Spitzer* observations based on alerts by MOA: MOA-2015-BLG-079, MOA-2015-BLG-237, and MOA-2015-BLG-267.
2. Event OGLE-2014-BLG-0613 was alerted in 2014; it has an extremely long timescale and has not reached baseline by the time this study started.
3. Event OGLE-2015-BLG-1136 was later identified as a cataclysmic variable (CV) rather than a microlensing event.
4. Six events show perturbations that can only be explained by stellar binaries: OGLE-2015-BLG-0060, OGLE-2015-BLG-0914, OGLE-2015-BLG-0968, OGLE-2015-BLG-1346, OGLE-2015-BLG-1368, and OGLE-2015-BLG-1212 (Bozza et al. 2016).
5. Events OGLE-2015-BLG-0022 and OGLE-2015-BLG-0244 show significant contamination of the xallarap effect (binary-source orbital motion).
6. Events OGLE-2015-BLG-1109 and OGLE-2015-BLG-1187 have impact parameters as seen from Earth $u_{0,\oplus} > 1$, which implies extremely low planet sensitivities.
7. The microlens parallax vector π_E of events OGLE-2015-BLG-1184 and OGLE-2015-BLG-1500 could not be measured because the time coverages by *Spitzer* are too short and the *Spitzer* light curves do not show any features of microlensing (Calchi Novati et al. 2015).
8. The microlens parallax vector π_E of event OGLE-2015-BLG-1403 could not be constrained because of the lack of the source color constraint.

Therefore, our raw sample contains 50 events. Information regarding their (equatorial and Galactic) positions and observations (by OGLE and *Spitzer*) is given in Table 1. Since all of these events lie in one of the four prime KMTNet fields, which were observed essentially continuously, their KMTNet cadences are virtually identical.

4. Methods

The sensitivity to planets of a microlensing event with a parallax measurement (and hence of an ensemble of such events) can be logically divided into two distinct problems. First, one must determine the probability function of the lens “distance” (defined more precisely below). Second, for each

allowed distance, one must determine the sensitivity to planets as a function of planet parameters, either the microlensing (q, s) or the physical parameters (m_p, a_\perp). These issues have been previously addressed separately by Calchi Novati et al. (2015), Yee et al. (2015b), and Zhu et al. (2015b). However, since this is the first measurement of sensitivity to the Galactic distribution of planets, we likewise present here the first integrated overview of the mathematics of this measurement. Moreover, based on this integration, we will identify some previously overlooked components of the analysis and also modify some past procedures.

Descriptions of the derivation of event solutions (Section 4.1), the estimation of lens distance and mass distributions (Section 4.3), and the computation of planet sensitivities (Section 4.4) follow immediately below.

4.1. Fourfold Solutions

The separation between Earth and the satellite perpendicular to the line of sight to the microlensing event, D_\perp , causes apparent changes in the angular lens–source separation $\Delta\theta = \pi_{\text{rel}} D_\perp / \text{au}$, and this in turn gives rise to different microlensing light curves. These light curves, as seen from Earth and from the satellite, appear to peak at different times t_0 and with different impact parameters u_0 (normalized to θ_E). In the approximation of rectilinear motion of Earth and the satellite (Refsdal 1966; Gould 1994; Graff & Gould 2002)

$$\pi_E \approx \frac{\text{au}}{D_\perp} (\Delta\tau, \Delta\beta), \quad (6)$$

where

$$\Delta\tau \equiv \frac{t_{0,\text{sat}} - t_{0,\oplus}}{t_E}; \quad \Delta\beta \equiv u_{0,\text{sat}} - u_{0,\oplus}. \quad (7)$$

Unfortunately, u_0 is a signed quantity (depending on whether the lens passes the source on its right or left; for sign definition see Figure 4 of Gould 2004), while only $|u_0|$ is directly measurable from the light curve. Therefore, satellite parallax measurements are subject to a fourfold degeneracy²¹

$$\pi_E \approx \frac{\text{au}}{D_\perp} (\Delta\tau, \Delta\beta_{\pm,\pm}), \quad (8)$$

where

$$\begin{cases} \Delta\beta_{+,+} \equiv +u_{0,\text{sat}} - u_{0,\oplus}, & (+,+) \text{ solution} \\ \Delta\beta_{+,-} \equiv -u_{0,\text{sat}} - u_{0,\oplus}, & (+,-) \text{ solution} \\ \Delta\beta_{-,-} \equiv -u_{0,\text{sat}} + u_{0,\oplus}, & (-,-) \text{ solution} \\ \Delta\beta_{-,+} \equiv +u_{0,\text{sat}} - u_{0,\oplus}, & (-,+) \text{ solution} \end{cases}. \quad (9)$$

In principle, higher-order effects in the light curve itself can break this degeneracy. At first order (in the polynomial expansion of Smith et al. 2003), it can be broken from the different Einstein timescales t_E measured from Earth and the satellite owing to their relative motion (even within the approximation of rectilinear motion) (Gould 1995). At third and fourth order, it can be broken owing to parallax effects from the accelerated motion of Earth (Gould 1992). In practice, however, these effects are usually quite weak. First, with current experiments, t_E is normally not independently measured

²¹ Here we adopt the following notation for the degenerate solutions: $[\text{sgn}(u_{0,\oplus}), \text{sgn}(u_{0,\text{spitz}})]$. See Zhu et al. (2015a) for the conversion between this notation and the one used in Calchi Novati et al. (2015).

from the satellite simply because the observational investment for this would be extremely high (Gaudi & Gould 1997a), and these resources are better applied to observing more events. Ground-based parallaxes are rarely measured because the Einstein timescales are typically small, $t_E < \text{yr}/2\pi$, so that third- and particularly fourth-order effects are very subtle. This indeed is the reason for going to space. Nevertheless, although these higher-order effects are small, they can contribute to breaking the degeneracy between well-determined but otherwise indistinguishable parallax solutions.

We search for and characterize the four solutions using the code developed in Zhu et al. (2016a). We first find a simple three-parameter (t_0, u_0, t_E) solution based on OGLE data. Next, we include *Spitzer* data, introduce two parameters $\pi_E n$ and $\pi_E e$, which are the two components of vector π_E along the north and east directions, respectively, and easily find one of the four parallax solutions by allowing χ^2 to go downhill. As per the usual convention, these parameters ($\pi_E n, \pi_E e, t_E$) are defined in the geocentric frame (Gould 2004).²² The location of the *Spitzer* satellite is extracted from the *JPL Horizons* website,²³ enabling a self-consistent quantification of the microlens parallax effect and the event timescale. In addition, there are two flux parameters for each data set, F_s and F_b . The former is the flux from the source, and the latter is the flux that is blended within the aperture and does not participate in the event. The model for the total flux observed at epoch t_i for data set j is then given by

$$F^j(t_i) = F_s^j \cdot A^j(t_i; t_0, u_0, t_E, \rho, \pi_E) + F_b^j. \quad (10)$$

Once a solution is found, we estimate the uncertainties of parameters via a Markov Chain Monte Carlo (MCMC) analysis, using the `emcee` ensemble sampler (Foreman-Mackey et al. 2013). The remaining three solutions are also easily found by seeding solutions at the locations expected based on Equation (8). In some cases, typically events with long timescales or events peaking near the beginning of the season, there is no local minimum at χ^2 surface for one or more solutions owing to strong parallax information from the ground. Within the mathematical formalism that follows, these other solutions can be thought of as “existing” but having very high $\Delta\chi^2$ relative to the best solution.

For each of the four solutions we then derive π_E , \tilde{v}_{hel} , the uncertainty of the latter quantity, and $\Delta\chi^2$ relative to the best solution. Here \tilde{v}_{hel} is the transverse velocity between the source and the lens projected onto the observer plane, after the correction from geocentric to heliocentric frames,

$$\tilde{v}_{\text{hel}} = \tilde{v}_{\text{geo}} + \mathbf{v}_{\oplus, \perp}; \quad \tilde{v}_{\text{geo}} = \frac{\text{au}}{t_E} \frac{\pi_E}{\pi_E^2}, \quad (11)$$

where $\mathbf{v}_{\oplus, \perp}$ is the velocity of Earth at the event peak and projected perpendicular to the directory of the event. To facilitate further discussions, we also define here the event timescale in the heliocentric frame

$$t'_E \equiv \frac{\tilde{r}_E}{\tilde{v}_{\text{hel}}}; \quad \tilde{r}_E \equiv \frac{\text{au}}{\pi_E}. \quad (12)$$

In deriving event solutions, we are able to incorporate “color constraints” (either *VI*[3.6 μm] or *IH*[3.6 μm]) into the fit. This is either very important or essential for the great majority of cases, as anticipated by Yee et al. (2015b). The naive idea of space-based parallaxes, as outlined by Refsdal (1966) and Gould (1994) and as captured by Equation (6), is that t_0 and u_0 will be measured independently from the satellite and Earth. However, such independent measurements are essentially impossible if the event is not observed over (or at least close to) peak. Hence, in the 2014 pilot program, exceptional efforts were made to observe over peak, which greatly restricted the number of events that could be targeted, given the short (~ 38 -day) observing window set by *Spitzer* Sun-angle restrictions and given the delays of 6 ± 3 days in observing targets (Figure 1 of Udalski et al. 2015b). However, based on experience in optical bands (Yee et al. 2012), Yee et al. (2015b) argued that, even if the peak were not observed from the satellite, it would be possible to recover $(t_0, t_E)_{\text{sat}}$ provided that the *Spitzer* source flux could be determined from a combination of (1) the measured source flux of the ground-based light curve, (2) the measured source color in ground-based bands ($V-I$ or $I-H$), and (3) a color-color relation (e.g., *VI*[3.6 μm] derived from field stars. In practice, we derive the $(I - [3.6 \mu\text{m}])$ from the measured color and color-color relation and then impose the 2σ limits of this measurement as hard constraints in the fit.

4.2. Galactic Model

4.2.1. Stellar Density Profile

The Galactic center has equatorial coordinates $(\alpha_{\text{GC}}, \delta_{\text{GC}}) = (17^{\text{h}}45^{\text{m}}37^{\text{s}}.224, -28^{\circ}56'10''.23)$ (Reid & Brunthaler 2004) and heliocentric distance $R_{\text{GC}} = 8.3$ kpc (Gillessen et al. 2009). The Sun is above the Galactic midplane ($z = 0$) by 27 pc (Chen et al. 2001), which corresponds to a tilt angle $\beta = 0^{\circ}.19$.

The total stellar number density n_* at given galactocentric coordinates (x, y, z) is the sum of contributions from the bulge and disk components

$$n_*(x, y, z) = n_{\text{B}}(x', y', z') + n_{\text{D}}(R, z). \quad (13)$$

We assume a triaxial G2 model for the bulge component (Kent et al. 1991; Dwek et al. 1995):

$$n_{\text{B}} = n_{\text{B},0} e^{-r_s^2/2}; \quad r_s \equiv \left\{ \left[\left(\frac{x'}{x_0} \right)^2 + \left(\frac{y'}{y_0} \right)^2 \right]^2 + \left(\frac{z'}{z_0} \right)^4 \right\}^{1/4}, \quad (14)$$

where $n_{\text{B},0} = 13.7 \text{ pc}^{-3}$, $x_0 = 1.59$ kpc, $y_0 = 424$ pc, and $z_0 = 424$ pc. These values are adopted from Robin et al. (2003). The coordinates (x', y', z') are derived by rotating the galactocentric coordinates (x, y, z) around the z -axis by $\alpha_{\text{bar}} = 30^{\circ}$ (e.g., Cao et al. 2013; Wegg & Gerhard 2013). The disk component in Equation (13) has the form (Bahcall 1986)

$$n_{\text{D}} = n_{\text{D},0} \exp \left[- \left(\frac{R - R_{\text{GC}}}{R_0} + \frac{|z|}{z_{\text{D},0}} \right) \right]. \quad (15)$$

Here $R \equiv \sqrt{x^2 + y^2}$, the local stellar number density $n_{\text{D},0} = 0.14 \text{ pc}^{-3}$, the scale length of the disk $R_0 = 3.5$ kpc, and the scale height of the disk $z_{\text{D},0} = 325$ pc (Han &

²² See a discussion of microlensing parallax in heliocentric frame in Calchi Novati & Scarpitta (2016).

²³ <http://ssd.jpl.nasa.gov/?horizons>

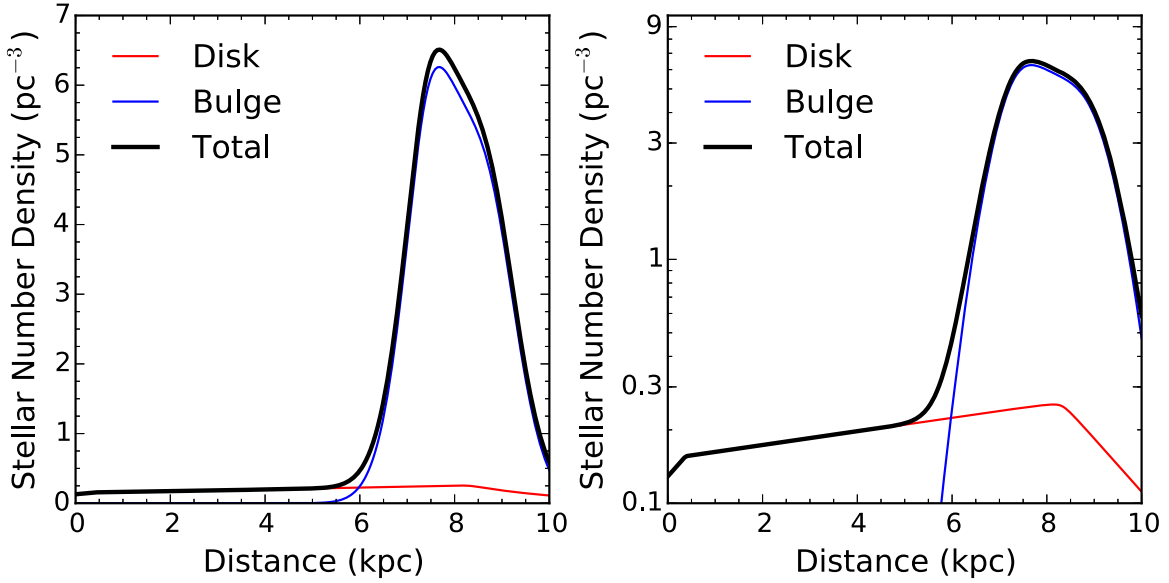


Figure 1. Stellar number density profile toward the Baade’s window for our adopted Galactic model, shown in linear scale on the left and logarithmic scale on the right.

Gould 1995). We show in Figure 1 the stellar number density profile toward the Baade’s window, which is approximately the center of microlensing fields.

4.2.2. Stellar Velocity Distribution

The mean stellar velocity at galactocentric coordinates (x, y, z) has the form

$$\mu_v(x, y, z) = \frac{n_B}{n_*} \mu_{v,B} + \frac{n_D}{n_*} \mu_{v,D}, \quad (16)$$

and the velocity dispersion is given by

$$\sigma_{v,i}^2(x, y, z) = \left(\frac{n_B}{n_*}\right)^2 \sigma_{v,i,B}^2 + \left(\frac{n_D}{n_*}\right)^2 \sigma_{v,i,D}^2 \quad (i = x, y, z). \quad (17)$$

We assume that the bulge stars have zero mean velocity and 120 km s^{-1} velocity dispersion along each direction ($\sigma_{v,i,B} = 120 \text{ km s}^{-1}$). The latter is derived from the proper-motion dispersion of bulge stars $\sigma_\mu = 3 \text{ mas yr}^{-1}$ (Poleski et al. 2013). Disk stars partake of the flat rotation curve with 240 km s^{-1} (i.e., $\mu_{v,z,D} = 0 \text{ km s}^{-1}$ and $\mu_{v,y,D} = 240 \text{ km s}^{-1}$; Reid et al. 2014), and their velocity dispersions are 18 and 33 km s^{-1} in the vertical (z) and rotation (y) directions, respectively. The Sun partakes of the same rotation curve and has a peculiar motion ($V_\odot = 12 \text{ km s}^{-1}$ and $W_\odot = 7 \text{ km s}^{-1}$; Schönrich et al. 2010) relative to the local standard of rest.

4.2.3. Stellar Mass Function

We choose two forms of the lens mass function (MF): (1) a flat MF with $d\xi(M_L)/d \log M_L \propto 1$ and (2) a Kroupa MF (Kroupa 2001)

$$\frac{d\xi(M_L)}{d \log M_L} \propto \begin{cases} M_L^{0.7}, & 0.013 < M_L/M_\odot < 0.08 \\ M_L^{-0.3}, & 0.08 < M_L/M_\odot < 0.5 \\ M_L^{-1.3}, & 0.5 < M_L/M_\odot < 1.3 \end{cases} \quad (18)$$

In both cases, no planetary lenses are included, and the upper end of the MF is truncated at $1.3 M_\odot$. As has been demonstrated in Calchi Novati et al. (2015) and will also be shown later, the choice of a different MF has essentially no effect on the result.

4.3. The Lens Distance and Mass Distribution

Following Calchi Novati et al. (2015), we define a lens “distance” parameter $D_{8.3}$ that is a monotonic function of π_{rel} ,

$$D_{8.3} \equiv \frac{\text{kpc}}{(\pi_{\text{rel}}/\text{mas}) + 1/8.3}. \quad (19)$$

This has the advantage that π_{rel} is much better constrained than the lens distance D_L (see Equation (5)), and it also informs us more of the Galactic population from which the lens is drawn. That is,

$$D_{8.3} \rightarrow D_L \quad (D_L \ll D_S), \quad (20)$$

$$(8.3 \text{ kpc} - D_{8.3}) \rightarrow D_{LS} \quad (D_{LS} \ll D_S), \quad (21)$$

where $D_{LS} \equiv D_S - D_L$. A determination that $D_{LS} \ll D_S$ is a much better indicator that the lens is in the bulge than the value of D_L (which in any case is less precisely known).

As discussed in Section 1, the lens distance parameter $D_{8.3}$ cannot be uniquely determined for the majority of events because of the lack of θ_E measurement. We therefore derive the Bayesian distribution of $D_{8.3}$ by imposing a Galactic model. As first pointed out by Han & Gould (1995), such a distribution of $D_{8.3}$ is fairly compact if π_E rather than θ_E (which gives μ_{rel}) can be measured. One can understand this by first approximating the Galactic disk lenses as moving exactly on a flat rotation curve and bulge sources as not moving. Then (also approximating the Sun as being at the local standard of rest),

$$\pi_{\text{rel}} \rightarrow \frac{\tilde{v}_{\text{hel}}}{\mu_{\text{sgrA*}}}, \quad (22)$$

where $\mu_{\text{sgrA*}}$ is the observed proper motion of the Galactic center and \tilde{v}_{hel} is the magnitude of \tilde{v}_{hel} from Equation (11). In fact, the velocities of both the sources and lenses are dispersed

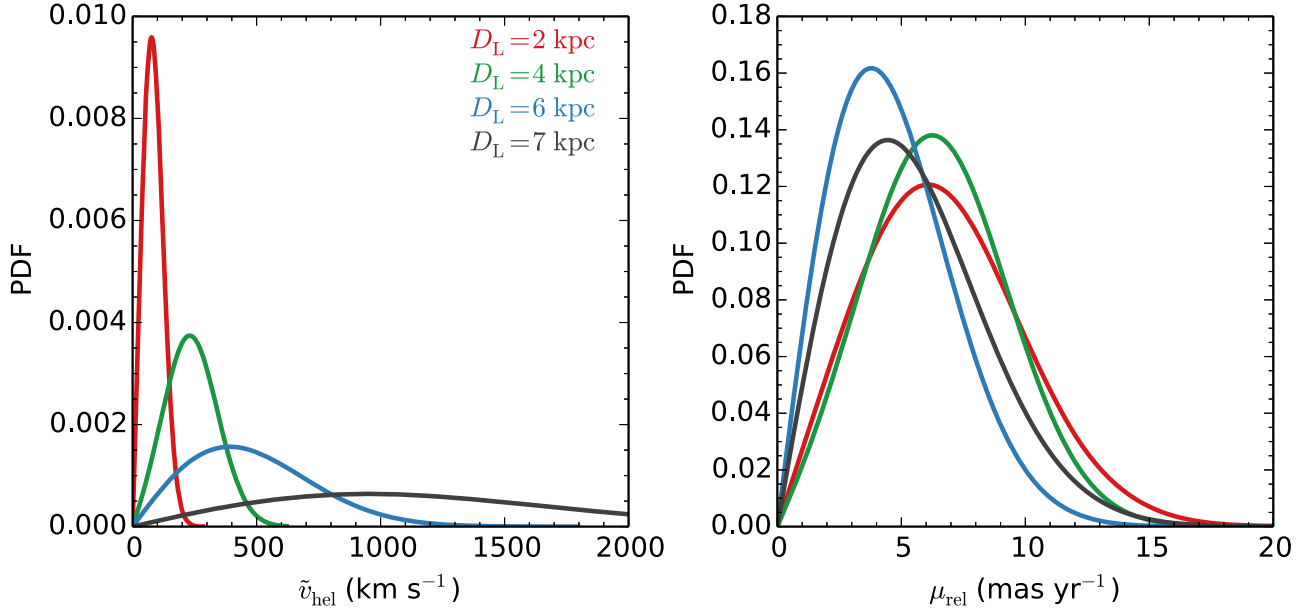


Figure 2. The (prior) probability distributions of \tilde{v}_{hel} (left panel) and μ_{rel} (right panel) for four lens distances $D_L = 2, 4, 6,$ and 7 kpc, under the Galactic model specified in Section 4.2. These distances represent typical lens distances at near disk, mid-disk, far disk, and bulge, respectively. For this illustration, the source has a fixed distance $D_S = 8.3$ kpc.

relative to this naive model. However, since these dispersions (projected on the observer plane) are typically small compared to the projection of the flat rotation curve, the probability distribution of π_{rel} (and therefore $D_{8.3}$) is typically compact. Then, since $M_L = \pi_{\text{rel}} / (\kappa \pi_E^2)$, M_L is also quite well measured.

To further illustrate this point under our adopted Galactic model, we show in Figure 2 the probability distributions of \tilde{v}_{hel} and μ_{rel} for several different lens distances. Here \tilde{v}_{hel} and μ_{rel} are the amplitudes of the two vectors $\tilde{\mathbf{v}}_{\text{hel}}$ and $\boldsymbol{\mu}_{\text{rel}}$, respectively, and these vectors are related to lens and source properties by

$$\tilde{\mathbf{v}}_{\text{hel}} = \frac{D_S}{D_{\text{LS}}} \mathbf{v}_{\text{L,gc}} - \frac{D_L}{D_{\text{LS}}} \mathbf{v}_{\text{S,gc}} - \mathbf{v}_{\odot,\text{gc}}, \quad (23)$$

and

$$\boldsymbol{\mu}_{\text{rel}} = \frac{\mathbf{v}_{\text{L,gc}} - \mathbf{v}_{\odot,\text{gc}}}{D_L} - \frac{\mathbf{v}_{\text{S,gc}} - \mathbf{v}_{\odot,\text{gc}}}{D_S}. \quad (24)$$

Here $\mathbf{v}_{\text{L,gc}}$, $\mathbf{v}_{\text{S,gc}}$, and $\mathbf{v}_{\odot,\text{gc}}$ are the galactocentric velocities of the lens, the source, and the Sun, respectively. Figure 2 demonstrates again that any knowledge of \tilde{v}_{hel} provides much more information of the lens distance than μ_{rel} could.

The distribution of $D_{8.3}$ is derived following a variant of the method in Calchi Novati et al. (2015). Here we provide the mathematical form of this derivation. For a fixed source distance D_S , the differential event rate of Galactic microlensing is given by

$$\frac{d^4\Gamma}{dD_L d \log M_L d^2 \boldsymbol{\mu}_{\text{rel}}} = n_{\text{L},*} D_L^2 (2\theta_E) \mu_{\text{rel}} f_{\mu}(\boldsymbol{\mu}_{\text{rel}}) \frac{d\xi(M_L)}{d \log M_L}. \quad (25)$$

Here $n_{\text{L},*}$ is the local stellar density at position (α, δ, D_L) , $f_{\mu}(\boldsymbol{\mu}_{\text{rel}})$ is the two-dimensional probability distribution function of the lens–source relative proper motion $\boldsymbol{\mu}_{\text{rel}}$, and $d\xi(M_L)/d \log M_L$ is the stellar MF in logarithmic scale.

Equation (25) can be rewritten in terms of microlensing observables $(D_{8.3}, t'_E, \tilde{v}_{\text{hel}})$,

$$\begin{aligned} \frac{d^4\Gamma}{dD_{8.3} dt'_E d^2 \tilde{v}_{\text{hel}}} &= \frac{d^4\Gamma}{dD_L d \log M_L d^2 \boldsymbol{\mu}_{\text{rel}}} \\ &\times \left| \frac{\partial(D_L, \log M_L, \boldsymbol{\mu}_{\text{rel}})}{\partial(D_{8.3}, t'_E, \tilde{v}_{\text{hel}})} \right| \cdot \quad (26) \\ &= 4n_{\text{L},*} \frac{D_L^4}{D_{8.3}^2} \mu_{\text{rel}}^2 f_{\tilde{v}}(\tilde{v}_{\text{hel}}) \frac{d\xi(M_L)}{d \log M_L} \end{aligned}$$

Here $f_{\tilde{v}}(\tilde{v}_{\text{hel}})$ is the two-dimensional probability function of $\tilde{\mathbf{v}}_{\text{hel}}$, which can be derived from Equation (23) under a given Galactic model. In the latter evaluation of Equation (26), we have substituted Equation (25) and the following Jacobian determinant:

$$\begin{aligned} \left| \frac{\partial(D_L, \log M_L, \boldsymbol{\mu}_{\text{rel}})}{\partial(D_{8.3}, t'_E, \tilde{v}_{\text{hel}})} \right| &= \left(\frac{D_L}{D_{8.3}} \right)^2 \frac{\mu_{\text{rel}}}{\tilde{v}_{\text{hel}}} \frac{1}{M_L} \left| \frac{\partial(M_L, \boldsymbol{\mu}_{\text{rel}})}{\partial(t'_E, \tilde{v}_{\text{hel}})} \right| \\ &= \left(\frac{D_L}{D_{8.3}} \right)^2 \frac{2\pi^2 \mu_{\text{rel}}}{\text{au}^2 t'^2_E} \quad (27) \end{aligned}$$

For a given set of $(t'_E, \tilde{v}_{\text{hel}})$, Equation (26) thus determines the relative (prior) probability distribution of $D_{8.3}$ at fixed D_S . This is then integrated over the posterior distributions of t'_E and \tilde{v}_{hel} from the light-curve modeling to yield the relative probability distribution of $D_{8.3}$ for a fixed D_S . To account for the variation in D_S , we average over all possible values of D_S (from $D_{\text{min}} = 6$ kpc to $D_{\text{max}} = 10$ kpc, assuming bulge sources), with each weighted by the number of available sources at that distance, $n_{\text{S},*} D_S^{2-\gamma} dD_S$. Here $n_{\text{S},*}$ is the local stellar density at (α, δ, D_S) , $D_S^2 dD_S$ is the volume between D_S and $D_S + dD_S$,

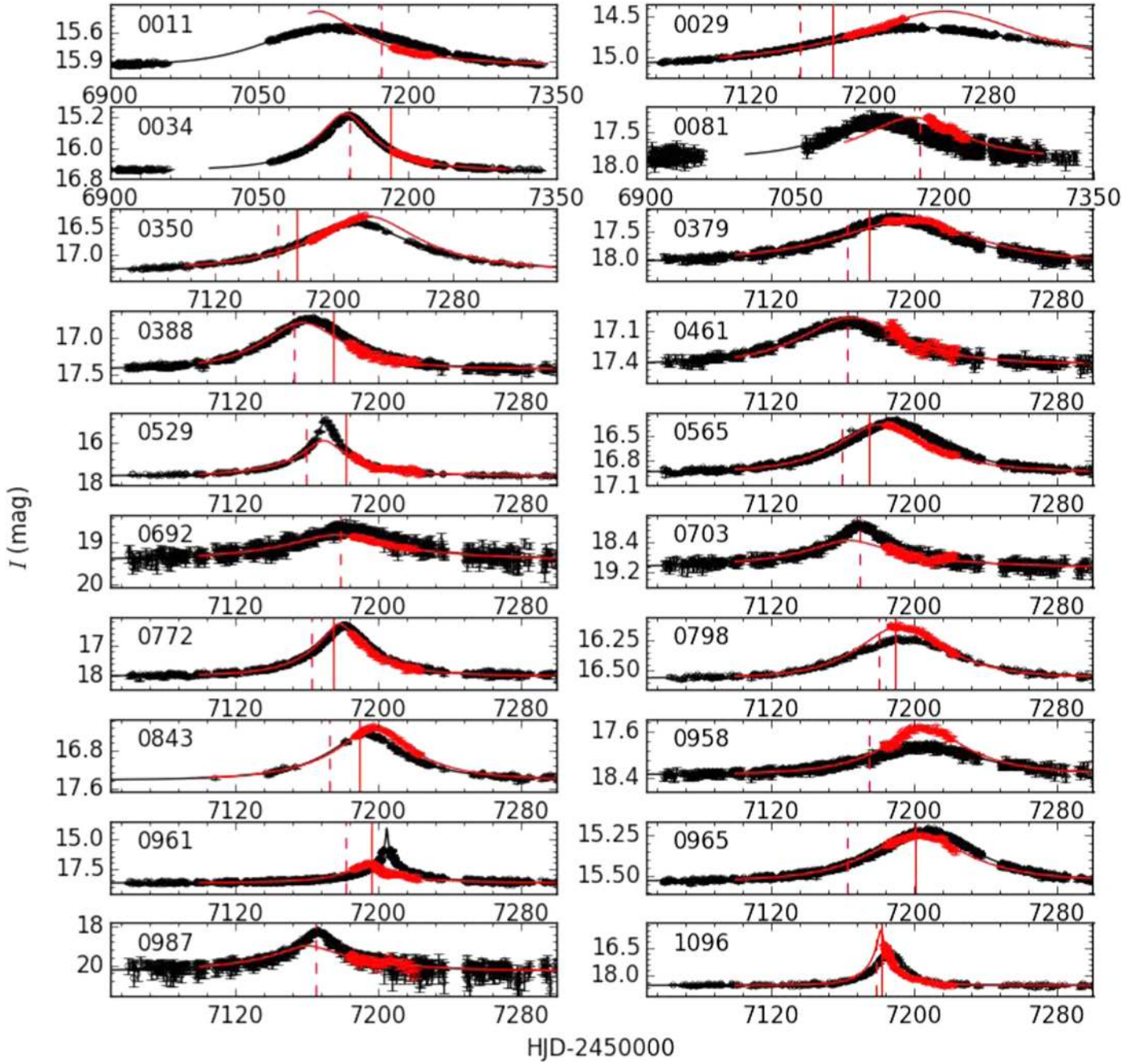


Figure 3. Ground-based (black) and space-based (red) data and best-fit models of the first 20 events in our sample. Here we only show the OGLE data for the ground-based part. KMTNet data have nearly continuous coverage with cadence ~ 10 minutes, as shown in Figure 6 for an example. The *Spitzer* data and light curves have been rescaled to the OGLE magnitude system according to Equation (34). For each event, the OGLE number is shown in the upper left corner, and the vertical red lines indicate the subjective (dashed) and objective (solid) selection dates. Note that models shown here are the ones with minimum χ^2 . Please refer to Table 2 for parameters and uncertainties of individual events. The data used to create this figure are available.

and $D_S^{-\gamma}$ is approximately the fraction of stars that have the measured apparent magnitude (Kiraga & Paczynski 1994). We choose $\gamma = 2.85$ for our sample, for reasons that are given in Appendix A. Then the non-normalized (“raw”) probability distribution of $D_{8.3}$ for the given solution is

$$P_{\text{raw}}(D_{8.3}) = \frac{\int_{D_{S,\min}}^{D_{S,\max}} \mathcal{P}(D_{8.3}|D_S) n_{S,*} D_S^{2-\gamma} dD_S}{\int_{D_{S,\min}}^{D_{S,\max}} n_{S,*} D_S^{2-\gamma} dD_S}, \quad (28)$$

where

$$\mathcal{P}(D_{8.3}|D_S) \equiv \int \frac{d^4\Gamma}{dD_{8.3} dt'_E d^2\tilde{\nu}_{\text{hel}}} \times P(t'_E|\text{Data}) P(\tilde{\nu}_{\text{hel}}|\text{Data}) dt'_E d^2\tilde{\nu}_{\text{hel}}. \quad (29)$$

In practice, we assume that the posterior distribution of t'_E , $P(t'_E|\text{Data})$, is a Dirac δ function and that the posterior distribution of $\tilde{\nu}_{\text{hel}}$, $P(\tilde{\nu}_{\text{hel}}|\text{Data})$, is a bivariate Gaussian

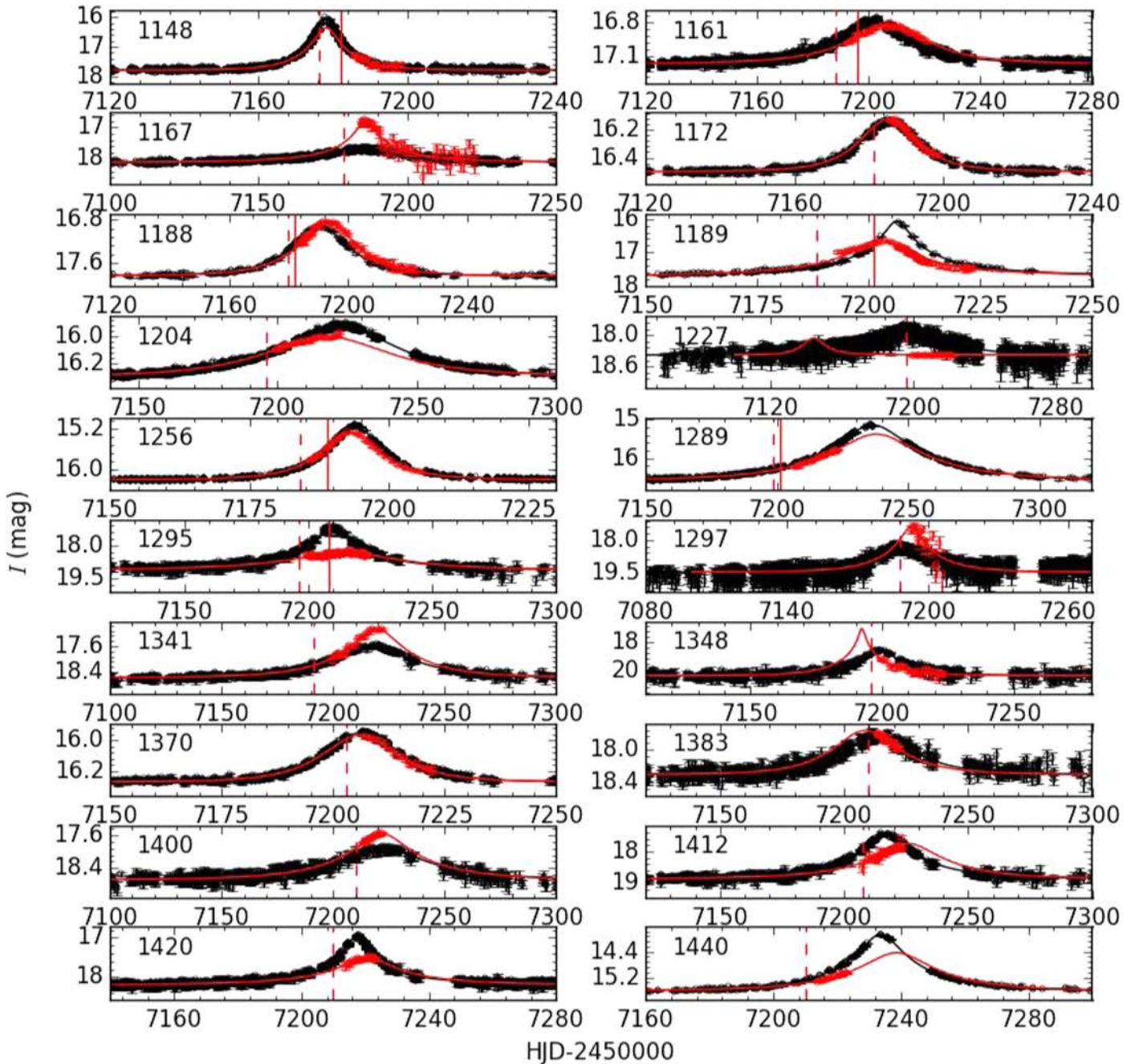


Figure 4. Ground-based (black) and space-based (red) data and best-fit models for events with OGLE number from 1148 to 1440. See caption of Figure 3 for detailed explanations. The data used to create this figure are available.

function whose covariance matrix is determined in Section 4.1. The former assumption is reasonable because t'_E (essentially t_E) is well measured in almost all events and especially because it is much better constrained than \tilde{v}_{hel} . The second assumption is adopted so that the above integration can be computed analytically (see Appendix B). We have nevertheless tested the validity of this assumption with some examples, by comparing the analytic result with numerical integration of the (non-Gaussian) true posterior distribution from MCMC.

To derive the distance distribution of one event, we must weight all degenerate solutions correctly. The weight contains two factors: (1) $\exp(-\Delta\chi^2/2)$, which is from the light-curve

modeling, and (2) π_E^{-2} , which is based on the so-called “Rich” argument. The Rich argument was originally pointed out by J. Rich (ca. 1997, private communication). It argues that, qualitatively, if $\pi_{E,+}$ (and so $\pi_{E,-}$) are much larger than $\pi_{E,+}$ (and $\pi_{E,-}$), then the former are likely spurious solutions. This is because the true solutions for events with small π_E are much more likely to be $\pi_{E,\pm\pm}$ solutions and can almost always generate spurious counterpart solutions $\pi_{E,\pm\mp}$ that are much larger. However, large π_E solutions can only rarely generate spurious small π_E solutions. Calchi Novati et al. (2015) quantified this argument and showed that solutions should be weighted by π_E^{-2} , although they nevertheless only applied this

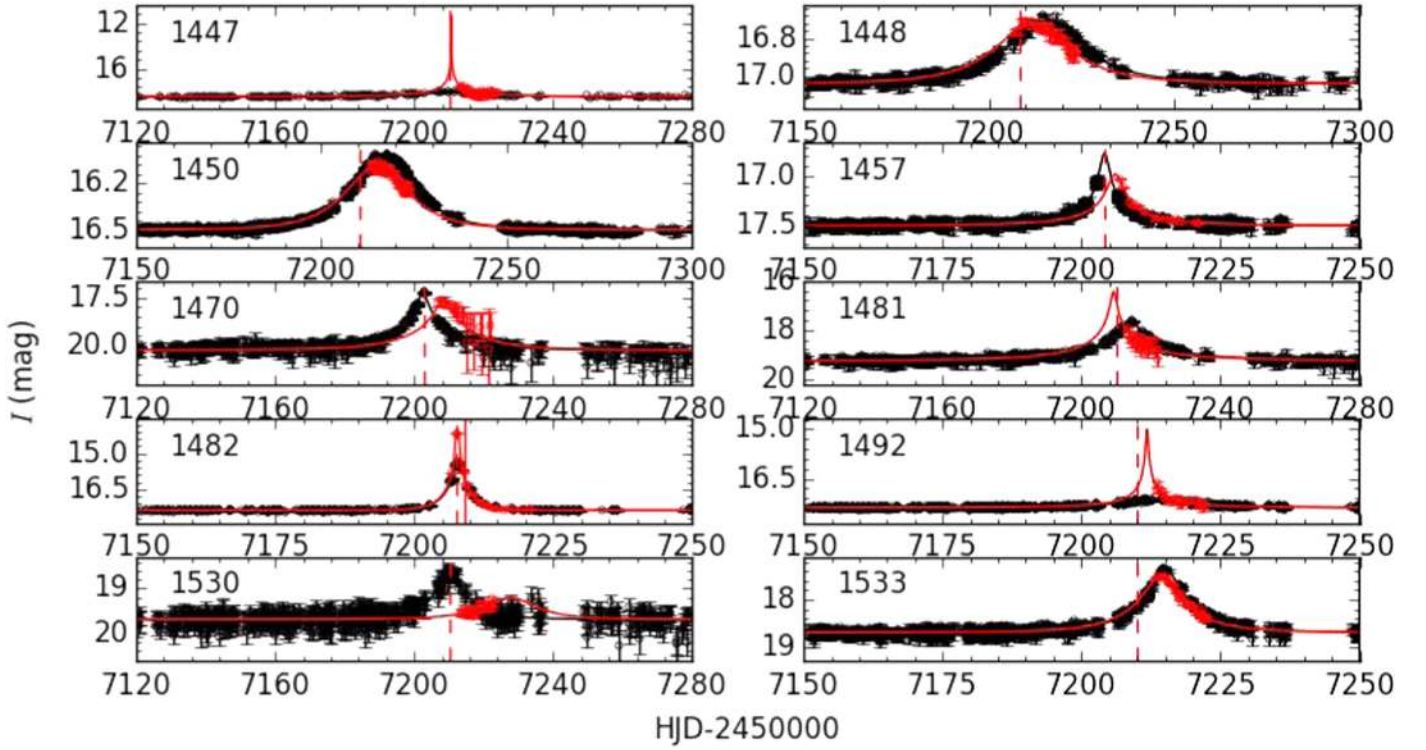


Figure 5. Ground-based (black) and space-based (red) data and best-fit models for the last 10 events in our sample. See the caption of Figure 3 for detailed explanations. The data used to create this figure are available.

weighting when the ratio of π_E between solutions was relatively large. Here, we carry the analysis of Calchi Novati et al. (2015) to its logical conclusion and apply this weighting uniformly to all events. The final normalized distribution of $D_{8.3}$ for each individual solution i is given by

$$P_i(D_{8.3}) = \frac{e^{-\Delta\chi_i^2/2} \pi_{E,i}^{-2} P_{i,\text{raw}}(D_{8.3})}{\mathcal{N}}, \quad (30)$$

where

$$\mathcal{N} \equiv \sum_{i=1}^4 \frac{e^{-\Delta\chi_i^2/2}}{\pi_{E,i}^2} \int P_{i,\text{raw}}(D_{8.3}) dD_{8.3}. \quad (31)$$

The lens mass distribution is derived in a similar way. One key equation involved is the following:

$$\frac{d^4\Gamma}{d \log M_L dt_E' d^2\tilde{v}_{\text{hel}}} = 4n_{L,*} D_L^4 f_{\tilde{v}}(\tilde{v}_{\text{hel}}) \frac{d\xi(M_L)}{d \log M_L} \frac{\mu_{\text{rel}}^3}{\tilde{v}_{\text{hel}}}. \quad (32)$$

The rest are almost identical to Equations (28) and (30), except for replacing $D_{8.3}$ with M_L (or $\log M_L$).

4.4. Planet Sensitivities

We apply the planet sensitivity code developed by Zhu et al. (2015b). The method was first proposed by Rhie et al. (2000)²⁴ and further developed by Yee et al. (2015b) and Zhu et al. (2015b) to incorporate space-based observations. Below we provide brief descriptions of the methods and the code, and interested readers can find more details in Yee et al. (2015b) and Zhu et al. (2015b).

The calculation of planet sensitivity requires a certain value for ρ , which is the angular source size θ_* normalized to θ_E , $\rho \equiv \theta_*/\theta_E$. The angular source size θ_* is estimated following the standard procedure, i.e., by comparing the positions of the source star and the red clump centroid on the color–magnitude diagram (Yoo et al. 2004). The determination of θ_E follows the prescription given by Yee et al. (2015b): for a given solution, we derive the transverse velocity \tilde{v}_{hel} using Equation (11) and choose $\mu_{\text{rel}} = 7 \text{ mas yr}^{-1}$ if \tilde{v}_{hel} favors a disk lens and $\mu_{\text{rel}} = 4 \text{ mas yr}^{-1}$ if \tilde{v}_{hel} favors a bulge lens; then $\theta_E = \mu_{\text{rel}} t_E$.

We first compute the planet sensitivity S as a function of planet-to-star mass ratio q and the planet/star separation s normalized to the angular Einstein radius θ_E . Twenty q values are chosen uniformly in logarithmic scale between 10^{-5} and 0.04, which correspond to a mass range from $1 M_{\oplus}$ to $13 M_J$ for a $0.3 M_{\odot}$ host. Twenty s values are chosen also uniformly in logarithmic scale between 0.3 and 3. Our choice of the “lensing zone” covers the region where microlensing is sensitive for nearly all the events. For each set of (q, s) , we generate 100 planetary light curves that have other parameters the same except for α , which is the angle between the source trajectory and the lens binary axis. For each simulated light curve, we then find the best-fit single-lens model using the downhill simplex algorithm, the goodness of which is quantified by χ_{SL}^2 . For events that were subjectively chosen and never met the objective criteria, we additionally find the deviation from the single-lens model in the ground-based data that were *released*²⁵ before the subjective chosen date t_{sub} . If this deviation is significant ($\chi^2 > 10$; Yee et al. 2015b), we consider the injected planet as having been noticeable and thus reject this α ,

²⁴ See also the other approach by Gaudi & Sackett (2000).

²⁵ All KMTNet data were released after the end of the season.

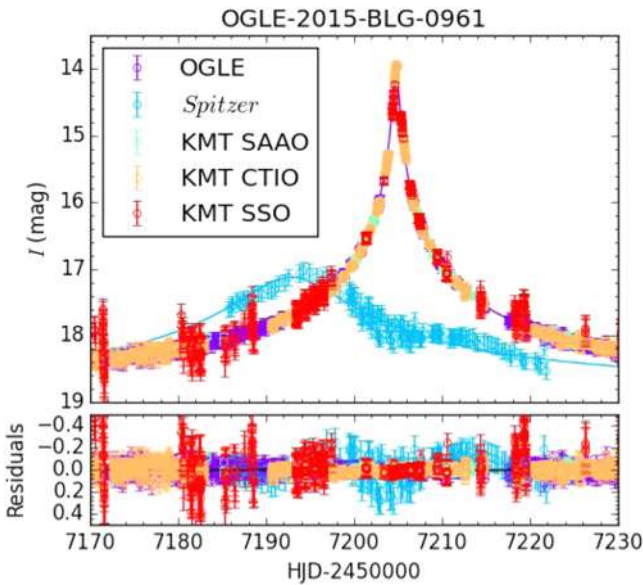


Figure 6. Light curves of event OGLE-2015-BLG-0961 as seen by *Spitzer* and from the ground. All ground-based data sets are shown here. The densely covered ground-based light curve shows no deviation from a point-lens event, which puts an upper limit on the planet-to-star mass ratio $q \lesssim 3 \times 10^{-4}$. The deviation in *Spitzer* light curve would require $q \gtrsim 2 \times 10^{-3}$. Therefore, the deviation in *Spitzer* data could only be caused by systematics.

regardless of how significant χ_{SL}^2 is. Otherwise, for these events and events that met objective criteria, we pass the simulated events to the anomaly detection filter. The sensitivity $S(q, s)$ is the fraction of α values for which the injected planets are detectable.

We adopt the following detection thresholds, which are more realistic than that used in Zhu et al. (2015b) and have been used in Poleski et al. (2016): $\chi_{\text{SL}}^2 > 300$ and at least three consecutive data points from the same observatory show $>3\sigma$ deviations (C1), or $\chi_{\text{SL}}^2 > 500$ (C2). C1 aims for capturing sharp planetary anomalies, and C2 is supplementary to C1 for recognizing the long-term weak distortions.

In principle, the planet sensitivities could be substantially different for the $\pi_{\text{E},\pm\pm}$ solutions compared to the $\pi_{\text{E},\pm\mp}$ solutions, because source trajectories as seen by Earth and *Spitzer* pass by the lens on the projected plane from the same side for the former, but on opposite sides for the latter (Zhu et al. 2015b). However, for the data sets under consideration in the present paper, which typically have several dozen observations per day from the ground and only one or a few per day from space, almost all the sensitivity comes from the ground observations. Hence, the sensitivities of the four degenerate solutions are almost identical. See Figure 6 of Poleski et al. (2016) for an example. The small differences between four solutions arise from the different values of ρ used in the computation, because $\rho = \theta_*/(\mu_{\text{rel}} t_{\text{E}})$ and the choice of μ_{rel} rely on the magnitude of π_{E} .

Current experiments are very far from having the ability to separately measure distance distributions for the individual (s , q). Hence, we also define the sensitivity to a given planet-to-star mass ratio q as

$$S(q) = \int S(q, s) d \log s. \quad (33)$$

This bears the assumption that the distribution of s is flat in logarithmic scale, which is reasonable according to recent

studies (e.g., Dong & Zhu 2013; Fressin et al. 2013; Petigura et al. 2013; Burke et al. 2015; Clanton & Gaudi 2016).

5. Results

5.1. Light Curves and Systematics

We present the ground-based and space-based light curves of each event in our sample in Figures 3–5. All data sets except OGLE have been rescaled to the OGLE I magnitude based on the best-fit model

$$\tilde{F}^j = \frac{F_s^{\text{OGLE}}}{F_s^j} (F^j - F_b^j) + F_b^{\text{OGLE}}. \quad (34)$$

We suppress KMTNet data sets in these plots and only show OGLE data for clarity. The reader can find an example event that demonstrates the much denser coverage of KMTNet in Figure 6.

The ground-based data of all 50 events in our sample can be well fitted by a single-lens model. However, the *Spitzer* data of several of them show deviations from this simple description. Some of these deviations are prominent, such as in OGLE-2015-BLG-0081, OGLE-2015-BLG-0461, OGLE-2015-BLG-0703, OGLE-2015-BLG-0961, and OGLE-2015-BLG-1189. However, we believe that these are due to unknown systematics in the *Spitzer* data rather than indications of companions to the lens. Below we provide two examples to demonstrate this point. Poleski et al. (2016) noticed a strong deviation in the *Spitzer* data of OGLE-2015-BLG-0448. Although they found that a lens companion with $q = 1.7 \times 10^{-4}$ could improve the single-lens model by $\Delta\chi^2 = 128$, they showed that even the best-fit binary-lens model could not remove all the deviations in the *Spitzer* data. Therefore, the trend in *Spitzer* data was likely caused by systematics rather than a physical signal from an additional lens object. This is especially true for OGLE-2015-BLG-0961. As shown in Figure 6, the ground-based data can be well fitted by a single-lens model with extremely high magnification ($u_{0,\oplus} \leq 0.005$ at 1σ level), which excludes any lens companions with $q \gtrsim 3 \times 10^{-4}$ if close to the Einstein ring (see Figure 13 below). The *Spitzer* data show a long-term deviation centered at the time when the event peaked from the ground. This long-term deviation, if attributed to a companion to the lens, could only be caused by the planetary caustic. With $u_{0,\text{spitz}} = 0.1$ and the position of planetary caustic at $|s - 1/s|$, the separation between the hypothetical lens companion and the primary lens should be $\log s = \pm 0.02$. Combining the duration of the deviation (10 days out of $t_{\text{E}} = 60$ days) and the width of the planetary caustic (Han 2006), we can put a limit on the companion mass ratio $q \gtrsim 2 \times 10^{-3}$. There do not exist any q values that could explain the nondetection in the ground-based data and the significant trend in *Spitzer* data. Therefore, the trend in *Spitzer* data is likely due to systematics in the *Spitzer* data reduction.²⁶

The systematics in *Spitzer* data can potentially affect the parallax measurements. However, it has been demonstrated that the influence is small in several published events. For example, Poleski et al. (2016) showed that the parallax parameters with

²⁶ In principle, the trend in *Spitzer* data can also be caused by binary sources. However, this scenario requires a secondary source that is nearly as faint as the primary source, but redder by 2.5 mag in $I - [3.6\mu\text{m}]$ or 1.6 mag in $V - I$. Such stars are extremely rare. Therefore, it is very unlikely that the trend is caused by binary sources.

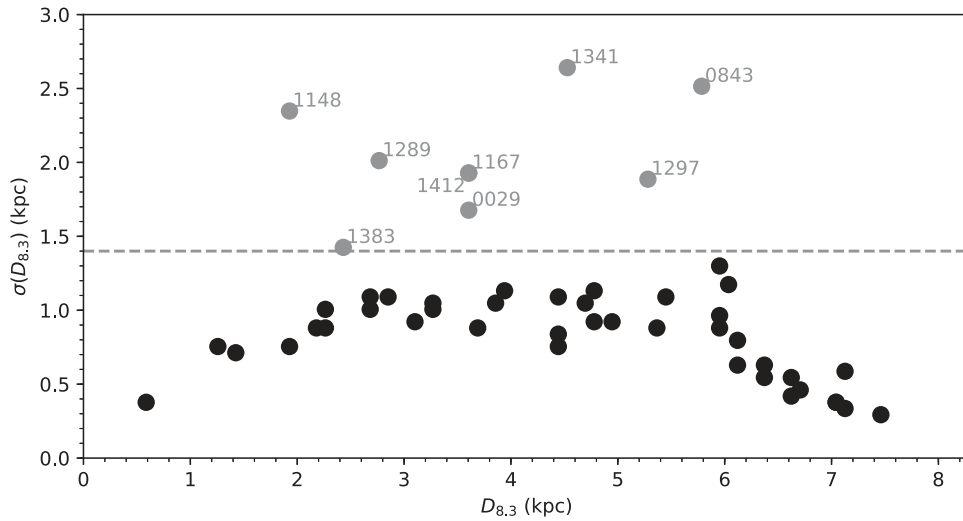


Figure 7. Median and 1σ uncertainty of the lens distance parameter $D_{8.3}$ (Equation (19)) of all 50 events in our raw sample. We exclude events with $\sigma(D_{8.3}) > 1.4$ kpc from the final statistical sample. This criterion was adopted based on examination of the distributions of $D_{8.3}$, which are shown in Figure 8. The OGLE numbers of all excluded events are labeled.

Table 2
Best-fit Parameters and Associated Uncertainties for the 50 Events in the Raw Sample

OGLE #	Solution	$\Delta\chi^2$	t_0	u_0	t_E	$\pi_{E,N}$	$\pi_{E,E}$	I_{base}^a	Blending	$I - [3.6\mu\text{m}]$
0011	(+, +)	0.0	7125.99(12)	0.8919(5)	80.96(26)	0.262(6)	0.104(4)	15.948	...	2.494(26)
	(-, -)	31.3	7125.53(10)	-0.8919(5)	74.0(3)	-0.403(9)	0.089(4)	15.948	...	2.529(24)
0029	(+, +)	0.0	7233.03(7)	0.7603(3)	101.77(11)	-0.1199(17)	-0.1192(17)	15.132	...	2.005(12)
0034	(+, +)	0.0	7140.37(3)	0.282(4)	64.2(4)	0.055(29)	-0.057(5)	16.559	0.009(18)	3.06(4)
	(-, -)	1.4	7140.37(3)	-0.283(3)	63.3(5)	-0.13(5)	-0.061(4)	16.559	0.001(15)	3.06(4)
0081	(+, +)	30.3	7135.4(4)	0.7014(14)	85.5(14)	-0.345(25)	-0.090(18)	17.892	...	2.758(14)
	(-, -)	0.0	7135.7(5)	-0.7037(13)	97.7(24)	0.475(28)	-0.130(21)	17.892	...	2.74(3)
0350	(+, +)	5.1	7214.86(12)	0.445(19)	70.7(20)	-0.049(3)	-0.068(7)	17.295	0.12(5)	2.626(21)
	(-, -)	0.0	7214.99(12)	-0.479(19)	66.7(18)	0.050(4)	-0.090(8)	17.295	0.01(5)	2.617(23)
	(-, +)	19.4	7214.50(11)	-0.448(17)	65.0(17)	0.567(20)	-0.205(9)	17.295	0.11(4)	2.595(23)
0379	(+, +)	2.8	7189.62(6)	0.448(15)	64.4(14)	0.003(11)	-0.098(7)	18.087	0.18(3)	2.61(3)
	(-, -)	0.0	7189.63(6)	-0.461(15)	62.7(14)	-0.001(13)	-0.119(7)	18.087	0.13(4)	2.59(5)
0388	(+, +)	0.0	7161.55(7)	0.508(21)	40.3(11)	0.11(3)	0.048(29)	17.425	0.25(4)	3.67(6)
	(-, -)	2.2	7161.55(7)	-0.518(23)	39.8(12)	-0.15(5)	0.018(29)	17.425	0.25(4)	3.65(6)
	(-, +)	2.1	7161.66(9)	-0.478(18)	46.5(11)	1.40(7)	-0.27(5)	17.425	0.32(3)	3.63(5)
0461	(+, +)	1.8	7161.27(19)	0.87(5)	41.6(17)	-0.20(5)	0.05(4)	17.414	-0.01(10)	1.76(7)
	(-, -)	0.0	7161.31(20)	-0.86(6)	42.9(23)	0.31(8)	0.05(4)	17.414	0.04(10)	1.71(9)

Note. For each event, we only include solutions that have $\Delta\chi^2 < 100$ from the lowest value. We present the total baseline magnitude in OGLE-IV I band, I_{base} , the blending fraction in I band, and the source $I - [3.6\mu\text{m}]$ color, rather than the flux parameters (F_s , F_b) of individual data sets. We assume no blending for events OGLE-2015-BLG-0011, OGLE-2015-BLG-0029, OGLE-2015-BLG-0081, OGLE-2015-BLG-0772, OGLE-2015-BLG-0798, OGLE-2015-BLG-1096, OGLE-2015-BLG-1188, OGLE-2015-BLG-1289, OGLE-2015-BLG-1297, OGLE-2015-BLG-1341, and OGLE-2015-BLG-1470, because free blending would lead to severely negative blending.

^a The uncertainty of I_{base} is ~ 1 mmag, primarily arising from OGLE-IV’s data-recording format. In addition, the calibration precision of OGLE-IV I band to the standard system, ~ 10 mmag, is not included here, on the basis that it does not affect the determination of microlensing parameters.

(This table is available in its entirety in machine-readable form.)

and without the systematic trend were almost identical. The agreement between orbital parallax and satellite parallax also indicates that the effect of systematics is less likely an issue (e.g., Udalski et al. 2015b; Han et al. 2017).

5.2. Event Parameters and Lens Distributions

We provide in Table 2 the best-fit parameters and associated uncertainties for solutions with $\Delta\chi^2 \leq 100$ of all 50 events.

Here $\Delta\chi^2$ is the difference between a given solution and the best solution for that event. With these, and following the method in Section 4.3, we derive the lens distance parameter $D_{8.3}$ and lens mass M_L distributions for every event in our raw sample.

Based on all event parameters and the subsequent lens distributions, we can now select events for our final statistical sample. The guideline is that only events with “detected parallax” can be included for the study of the Galactic

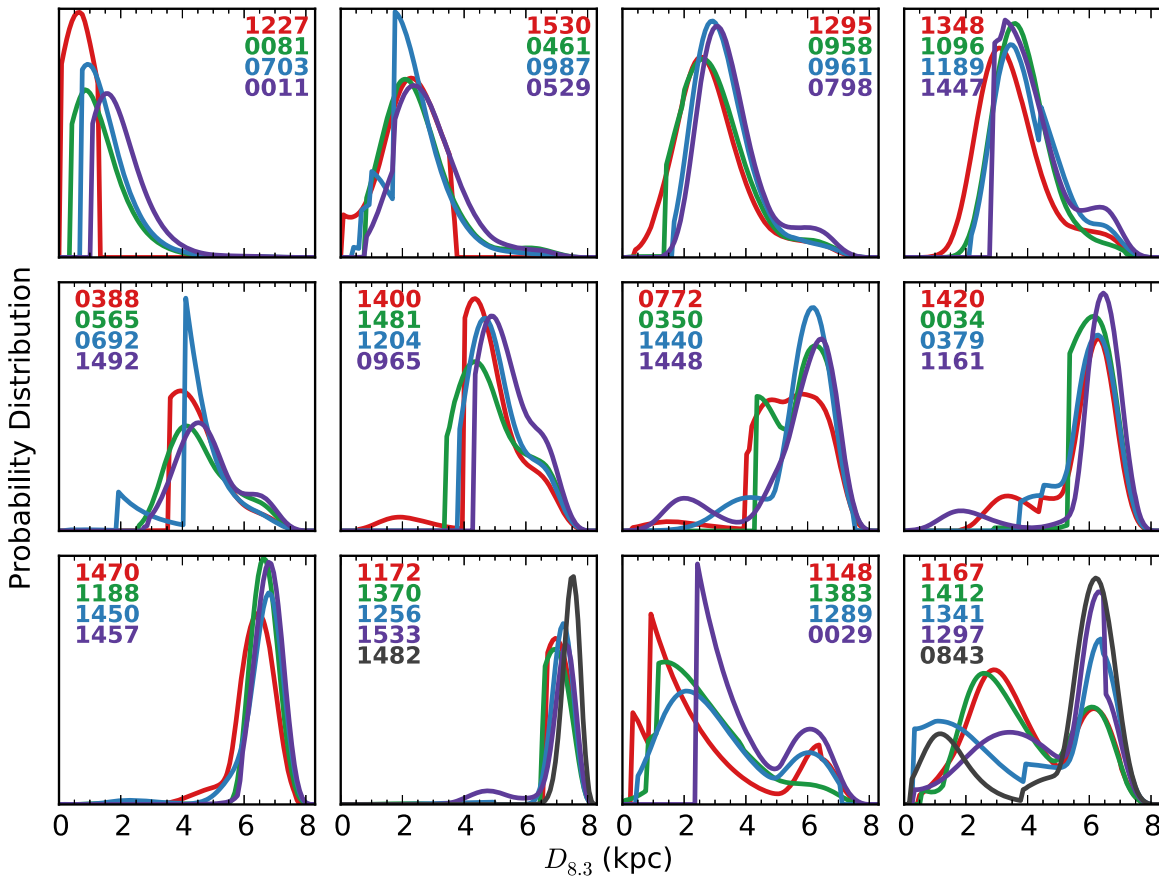


Figure 8. Distributions of lens distance parameter $D_{8,3}$ for all 50 events in our raw sample. Events in the last two panels (bottom right) are excluded from the final sample because of their broad $D_{8,3}$ distribution. Events included in the final sample, as well as events excluded from the final sample, are shown in the order of increasing median $D_{8,3}$.

distribution of planets, as Yee et al. (2015b) pointed out. At first sight, the above guideline seems to suggest a criterion on the measurement uncertainty of π_E . However, such an approach would be problematic, in particular because the uncertainty of π_E is determined for individual solutions, but decisions have to be made for individual events, which generally have more than one solution. As shown in Table 2, the (\pm, \mp) solutions are in general better constrained than the (\pm, \pm) solutions, so even though they are statistically disfavored by the Rich argument, they are more likely to survive if a cut on the detection significance of π_E is applied. Although it is possible to design a criterion for choosing events that balances the two opposite factors, a better approach is to choose events based on the distance parameter $D_{8,3}$ and its associated uncertainty $\sigma(D_{8,3})$. This is because only events with well-determined distances contribute to the measurement of the Galactic distribution of planets.

We show in Figure 7 the median value and the 1σ uncertainty of the lens distance parameter $D_{8,3}$ derived for each event in our raw sample. Here the 1σ uncertainty is the half-width of a 68% confidence interval centered on the median $D_{8,3}$. By visually inspecting the $D_{8,3}$ distributions of all 50 events, which are shown in Figure 8, we decide to use $\sigma(D_{8,3}) \leq 1.4$ kpc as the criterion for claiming a parallax detection and thus for any event to be included in the final sample. We end up with 41 events in the final sample. The nine events that are excluded all have broad distributions of $D_{8,3}$, even though some of them have very good measurements of π_E (e.g., OGLE-2015-BLG-0029, OGLE-

2015-BLG-0843, OGLE-2015-BLG-1167). The broad distribution of $D_{8,3}$ arises from the atypical magnitude and direction of \tilde{v}_{hel} . When combined with the Galactic model, the former favors near- to mid-disk lenses, while the latter favors bulge lenses.

The derived lens masses and the fractional uncertainties are shown in Figure 9. As expected, events that do not show compact $D_{8,3}$ distributions do not have well-constrained mass estimates either. For events in our final sample, the typical uncertainty of the lens mass estimate is 20%, regardless of whether it is substellar or not. In particular, we note that the lens mass estimate of OGLE-2015-BLG-1482 agrees reasonably well ($\leq 2\sigma$) with the direct mass measurement from the finite-source effect (S.-J. Chung et al. 2017) as a demonstration that the mass estimate method employed here is valid. The derived lens mass distributions of all 50 events are presented in Figure 10.

We show in Figure 11 the cumulative distributions of event timescales t_E and impact parameters $u_{0,\oplus}$ as seen from the ground, and we compare them with those in the OGLE-III microlensing event catalog (Wyrzykowski et al. 2015), which can be considered to be complete and uniform for our purpose. Because different solutions have only slightly different t_E and $u_{0,\oplus}$, we simply take values of the solution with lowest χ^2 . For the timescale t_E distribution, we notice that events in our final sample are more concentrated within 10–100 days than events in the OGLE-III catalog. The lower limit comes into play because there is a 3- to 9-day lag between events being selected and events getting observed by *Spitzer* (see Figure 1 of Udalski

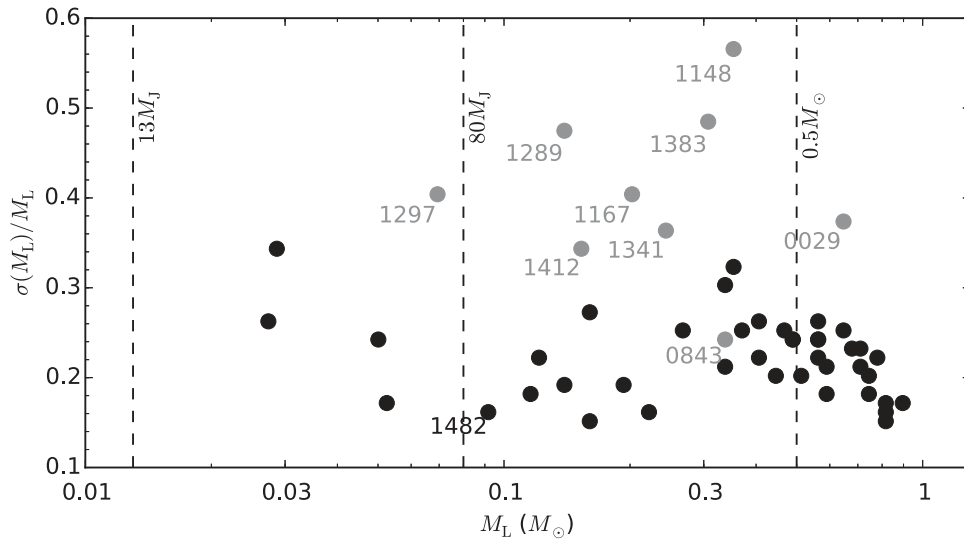


Figure 9. Median and fractional uncertainty of the lens mass M_L of all 50 events in our raw sample. Events that are excluded from the final sample based on the $\sigma(D_{8.3})$ criterion are shown in gray and have their OGLE numbers labeled. The vertical dashed lines indicate three characteristic masses, $13 M_J$, $0.08 M_\odot$, and $0.5 M_\odot$, respectively. Event OGLE-2015-BLG-1482 has direct mass measurement from the finite-source effect, $M_L = 0.10 \pm 0.02 M_\odot$ or $0.06 \pm 0.01 M_\odot$ (S.-J. Chung et al. 2017). Our Bayesian estimate of the mass agrees with the direct measurement pretty well ($\leq 2\sigma$).

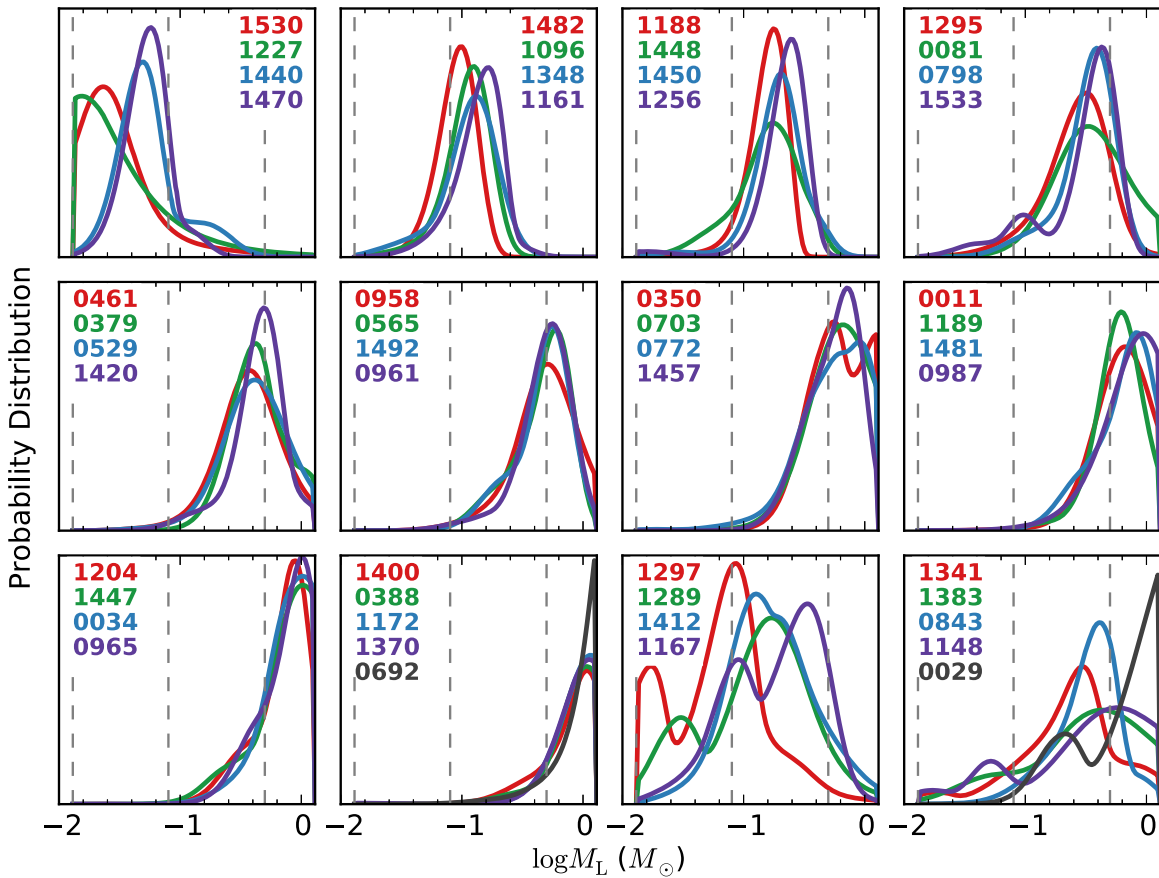


Figure 10. Distributions of lens mass M_L for all 50 events in our raw sample. Events in the last two panels (bottom right) are excluded from the final sample because of their broad $D_{8.3}$ distribution. Events included in the final sample, as well as events excluded from the final sample, are shown in the order of increasing M_L median. The vertical dashed lines indicate three characteristic masses, $13 M_J$, $0.08 M_\odot$, and $0.5 M_\odot$, respectively.

et al. 2015b). The lack of extremely long timescale ($t_E \gtrsim 100$ days) events comes as a consequence of our event selection criteria, because a substantial brightness change ($\gtrsim 0.3$ mag) during the ~ 40 -day *Spitzer* bulge window is required in order to detect the parallax effect (Yee et al. 2015b). Although the

events in our sample (and subsequent larger samples) have a biased t_E distribution, this bias applies to both events with and without planet detections in the same way. Therefore, it will not affect the statistical studies of the Galactic distribution of planets. The *Spitzer* sample u_0 distribution shows similar

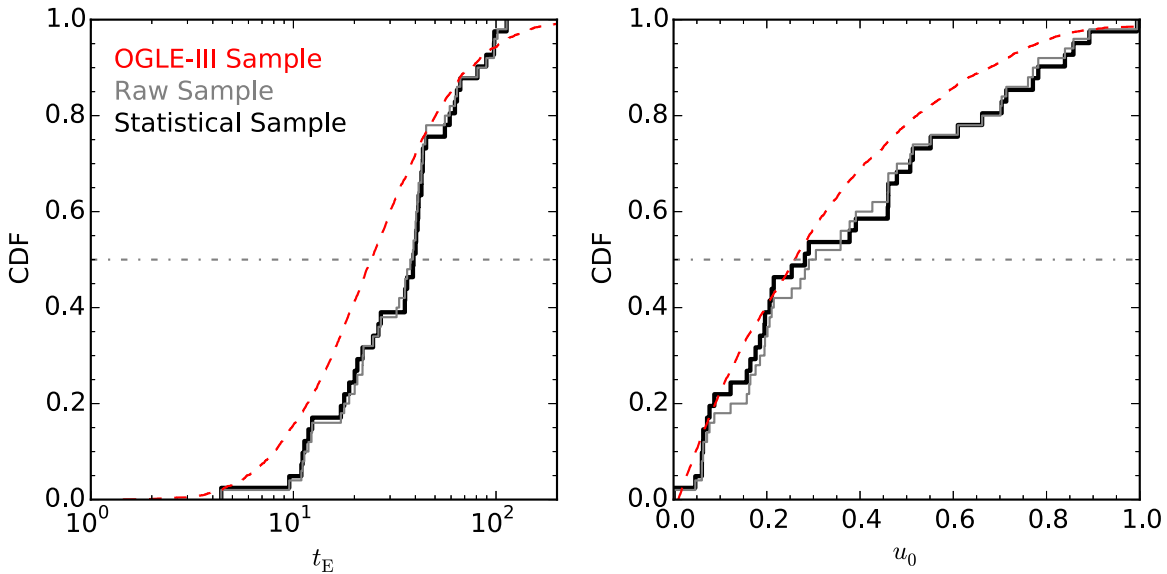


Figure 11. Cumulative distributions of timescale t_E and impact parameter u_0 for events in our sample (black solid curves) and in the OGLE-III sample (red dashed curves) from Wyrzykowski et al. (2015). Events with $u_0 < 0.01$ in the OGLE-III sample have been excluded because of their unreliable parameters (Gould et al. 2010). For each event in our sample, the values are chosen from the solution that has the lowest χ^2 , although the differences between different solutions are small. The gray horizontal lines indicate the median level.

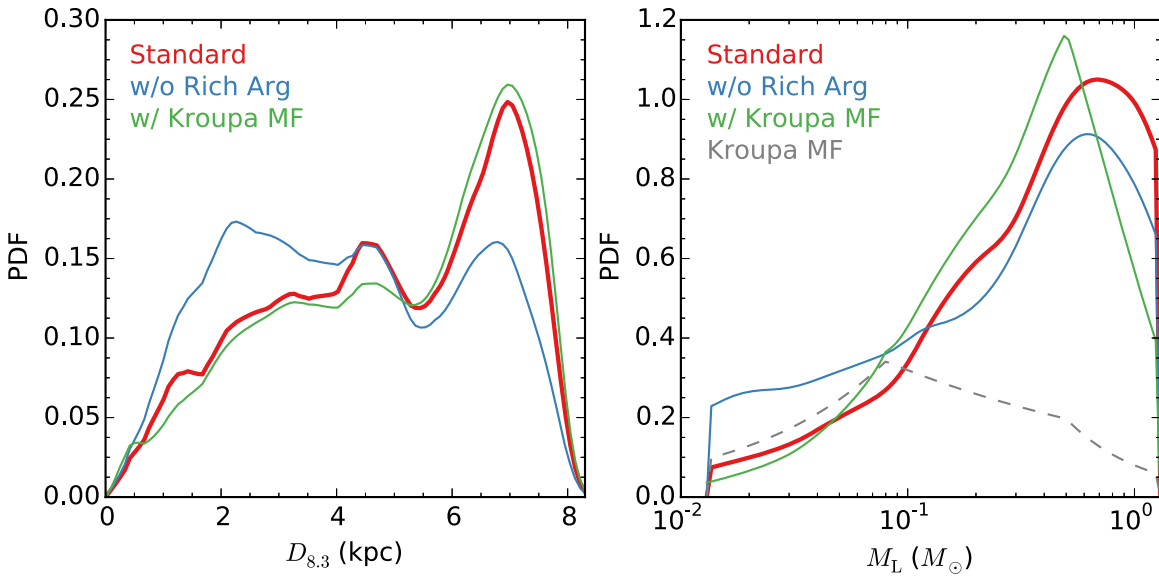


Figure 12. Differential probability distribution functions of lens distance parameter $D_{8.3}$ (left panel) and lens mass M_L for the 41 events in our sample. We choose the results with a flat MF (in $\log M_L$) and Rich argument as “standard,” but we also consider cases in which the Rich argument is removed (labeled “w/o Rich Arg”) and the MF is replaced with the Kroupa MF (labeled “w/ Kroupa MF”), respectively. Note, in particular, that changing the MF has almost no effect on the inferred distances. In the right panel we also illustrate the Kroupa MF (Equation (18)), employing an arbitrary normalization for this purpose.

overall morphology to that of the OGLE-III catalog but is more uniform, which indicates that it shows less magnification bias. This again reflects the fact that OGLE-III detections are possible based on a few days of relatively magnified sources, whereas *Spitzer* selections are delayed by 3–9 days.

We show in Figure 12 the distributions of lens distance parameter $D_{8.3}$ and lens mass M_L , which are averaged over all 41 events in the final sample. We consider the influences of the Rich argument and a different choice of stellar MF (e.g., Kroupa MF). As expected (see Section 4.1; see also Calchi Novati et al. 2015), the lens distance distribution is biased toward more nearby and therefore lower-mass lenses, if the

Rich argument is not taken into account. The different choices of the stellar MF have a marginal effect, especially on the lens distance distribution. Our result demonstrates, for the first time, that the peak of the microlens mass distribution is at $0.5 M_\odot$ and that the majority microlensing events are caused by M dwarfs.

5.3. Planet Sensitivities and Constraints on Planet Distribution Function

We present in Figures 13 and 14 the planet sensitivity plots of individual events in our final sample. Events are divided

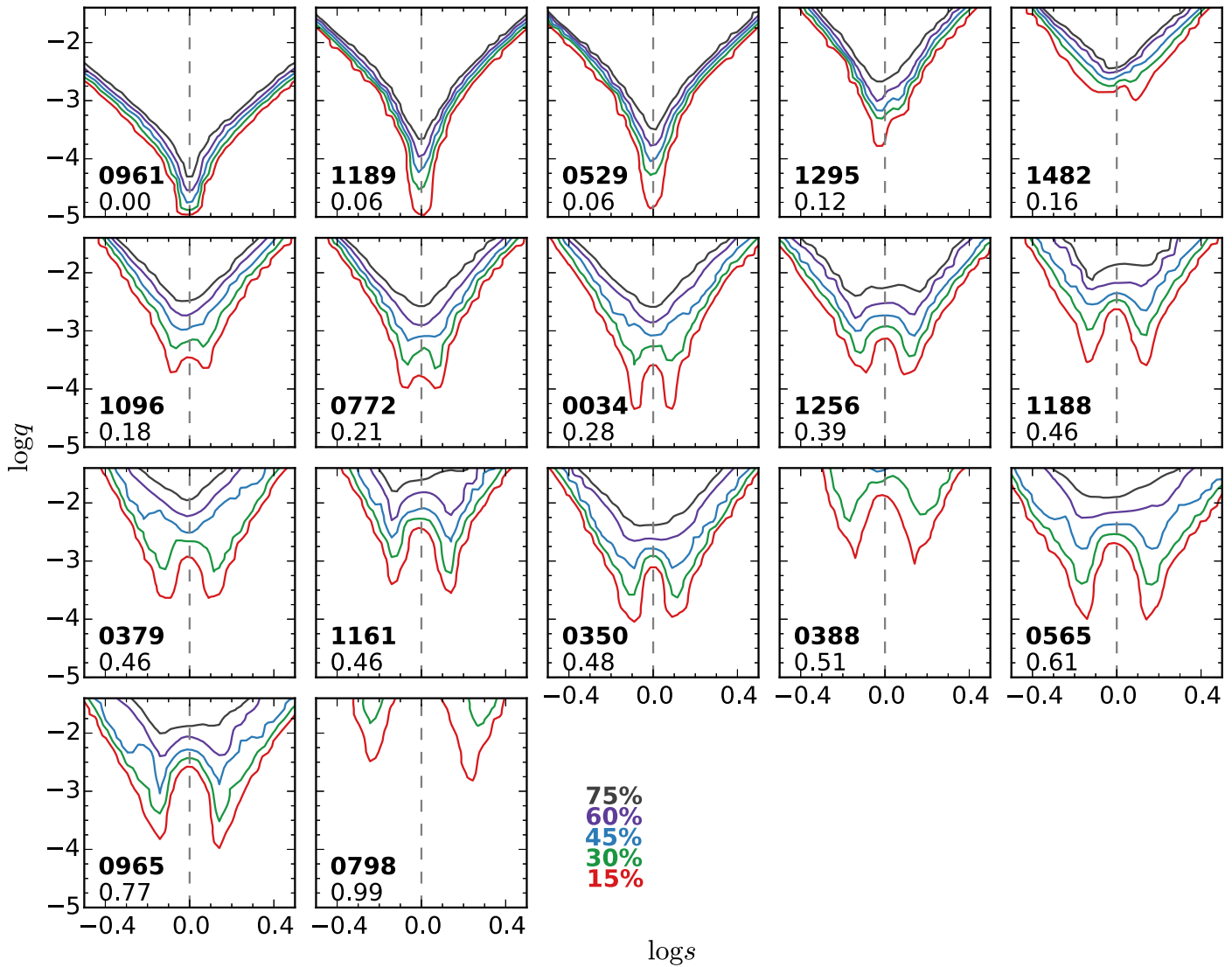


Figure 13. Planet sensitivity curves of the 17 objectively selected events, sorted by the impact parameters. The OGLE number and the impact parameter are provided in the lower left corner of each plot. The colors represent the curves with different sensitivities in $S(q, s)$. For simplicity, we only show the sensitivity curves for the (+, +) solution, regardless of how many solutions we calculated. The difference between sensitivity curves of different solutions is small.

according to their final status of *Spitzer* selections, with objectively selected events shown in Figure 13 and subjectively selected events shown in Figure 14. For all objective events and most subjective events, the sensitivity curves are smooth and triangle-like, with either a single horn (for relatively high magnification events; see also Gould et al. 2010) or double horns (for relatively low magnification events; see also Gaudi et al. 2002). In the remaining subjective events, however, the sensitivity curves show discontinuity especially at large q values. This was caused by the way that the planet sensitivity of a subjectively chosen event was computed. As described in detail in Yee et al. (2015b) and Zhu et al. (2015b) and summarized in Section 4.4, for events that were chosen subjectively and never met the objective selection criteria, all (hypothetical) planet detections must be censored from the statistical sample if they would have betrayed their existence in the data that were released before the subjective selection date t_{sub} . This has only a marginal effect if t_{sub} is well before the event peak $t_{0,\oplus}$, because the bulk of planet sensitivities come

from the region near the peak ($|t - t_{0,\oplus}| \lesssim u_{0,\oplus} t_E$). If t_{sub} is close to $t_{0,\oplus}$, then the above procedure could affect the final sensitivity curves significantly. In particular, planets that are more massive and closer to the Einstein ring are more easily excluded in the sensitivity computation; for given combinations of q and s , some choices of α are more easily discarded as well. As an example, we show in Figure 15 the χ^2 maps for three different q values for two events, OGLE-2015-BLG-0987 and OGLE-2015-BLG-1189, which have similar impact parameters $u_{0,\oplus}$ but show very different sensitivity curves.

We provide constraints on the planet distribution function, based on the null detection in our sample. We adopt as the planet distribution function the form

$$\frac{dN}{d \log q} = \mathcal{A} \left(\frac{q}{q_{\text{ref}}} \right)^\alpha, \quad (35)$$

and we choose $q_{\text{ref}} = 5 \times 10^{-4}$, which is the typical q value of microlensing planets (e.g., Gould et al. 2010). We first show in

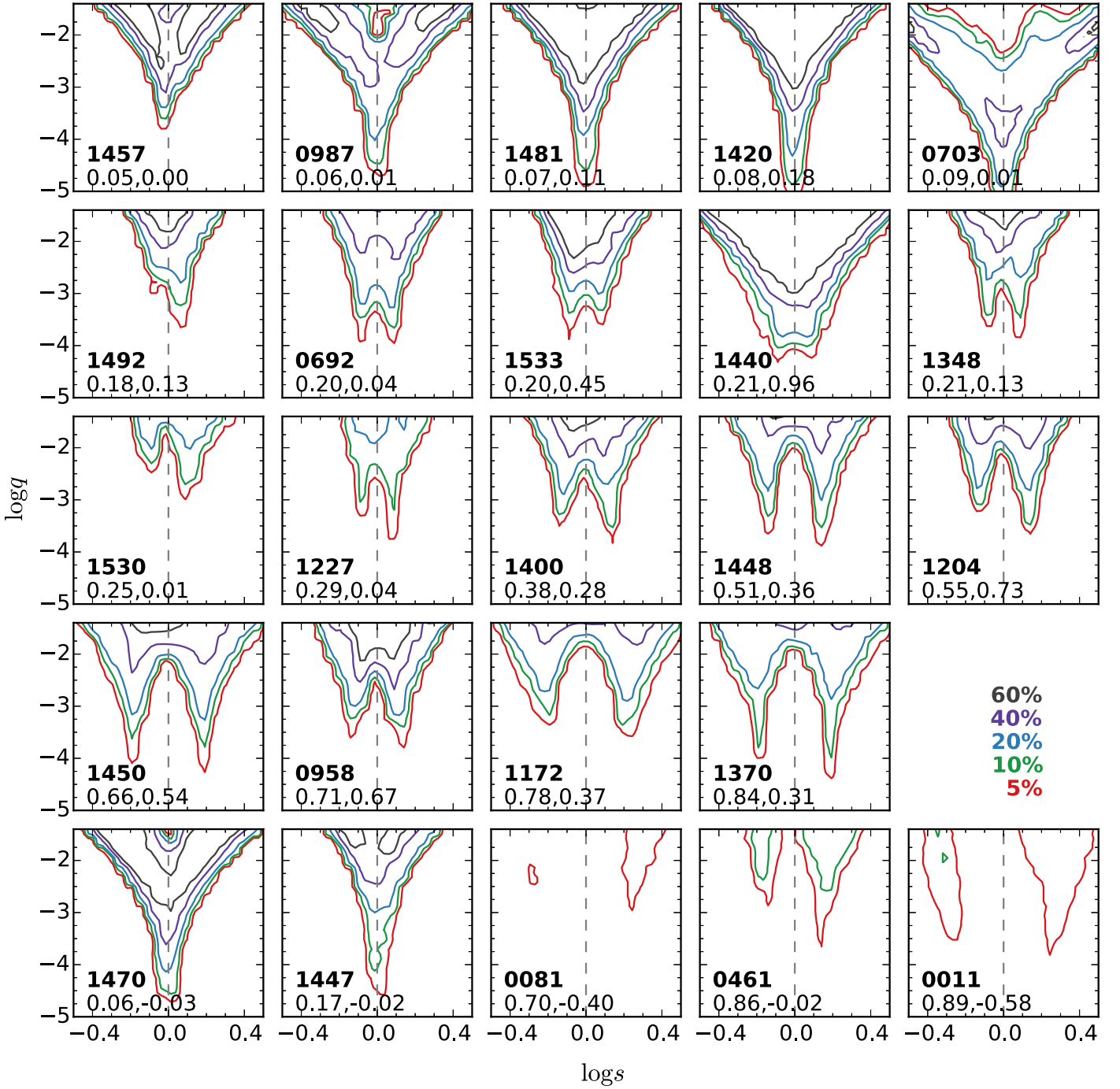


Figure 14. Planet sensitivity curves of the 24 subjectively selected events. These events are grouped into two categories: events selected before the peak as seen from the ground (top four rows), and events selected after the peak as seen from the ground (bottom row). In each category, events are shown in the order of increasing impact parameter. In each panel, we indicate the OGLE number (in bold), impact parameter u_0 , and the subjective selection relative to the peak, $(t_0 - t_{\text{sub}})/t_E$, in the lower left corner.

the left panel of Figure 16 the sensitivity curves averaged over the 41 events in the final sample. Assuming Poisson-like noise and that “planets” should have $q \leq 10^{-2}$ (to be consistent with previous studies; e.g., Gould et al. 2010), we are able to derive the constraints on the slope of the planet MF α and the normalization factor \mathcal{A} based on the null detection in our sample. The results are shown in the right panel of Figure 16. Our constraints are consistent, at the 2σ level, with previous statistical studies based on samples of microlensing planets

(Gould et al. 2010; Shvartzvald et al. 2016; Suzuki et al. 2016). In particular, we find $\mathcal{A} < 0.49$ at the 95% confidence level for a flat ($\alpha = 0$) planet MF, which is consistent with the result ($\mathcal{A} = 0.36 \pm 0.15$) from Gould et al. (2010).

5.4. Galactic Distribution of Planets

We derive the cumulative distribution of planet sensitivities of our sample based on the lens distribution $P(D_{8.3})$ and the planet sensitivity $S(q)$. The results are presented here in terms

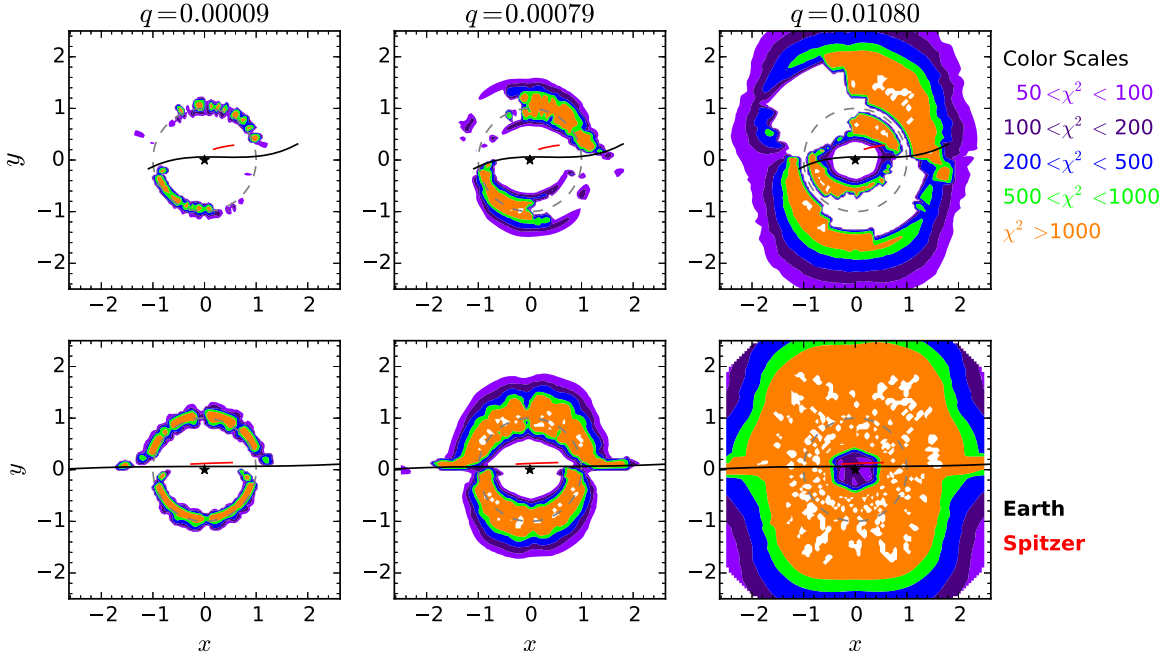


Figure 15. Detectabilities (i.e., the χ^2 deviation from a single-lens light curve) of three q values at different positions (x,y) for two events OGLE-2015-BLG-0987 (top panels) and OGLE-2015-BLG-1189 (bottom panels). These two events have similar impact parameters $u_{0,\oplus} \approx 0.06$, but their sensitivities to planets are quite different owing to their different selection statuses. See the text for more explanations. In each panel, the red and black curves indicate the source trajectories seen by *Spitzer* and from the ground, respectively, and the gray dashed curve indicates the position of Einstein ring.

of both the planet-to-star mass ratio q ,

$$C_q(D_{8.3}) = \frac{1}{C_q(R_{GC})} \sum_{ij} \int_0^{D_{8.3}} P_i^j(D') dD' \times \int_{q_{min}}^{q_{max}} S_i^j(q) d \log q, \quad (36)$$

and the planet mass m_p ,

$$C_m(D_{8.3}) = \frac{1}{C_m(R_{GC})} \times \sum_{ij} \int_0^{D_{8.3}} P_i^j(D') dD' \int_{q_{min}(D')}^{q_{max}(D')} S_i^j(q) d \log q. \quad (37)$$

Here $P_i^j(D_{8.3})$ and $S_i^j(q)$ are the lens distance distribution and the planet sensitivity for solution i of event j , respectively. In Equation (36), we choose $q_{min} = 10^{-5}$ and $q_{max} = 10^{-2}$. In Equation (37), we solve for the boundaries on q for individual $D_{8.3}$ values that lead to the planet mass ranging from $1 M_{\oplus}$ to $3 M_J$. These two distributions are normalized so that $C(R_{GC}) = 1$. The results are shown as the solid black curves in Figure 17.

In terms of the Galactic distribution of planets, we derive the ratio of planets in the bulge to planets in the disk (to which our survey is sensitive),

$$\eta_{b2d} \equiv \frac{\int_0^{R_{GC}} C'(D_{8.3}) f_B(D_{8.3}) d D_{8.3}}{\int_0^{R_{GC}} C'(D_{8.3}) [1 - f_B(D_{8.3})] d D_{8.3}}. \quad (38)$$

Here $C'(D_{8.3})$ is the derivative of $C(D_{8.3})$, and $f_B(D_{8.3})$ is the contribution of bulge events (lens in the bulge) to all events at

given $D_{8.3}$, which is given by

$$f_B(D_{8.3}) = \frac{\int_{D_{S,min}}^{D_{S,max}} n_B(D_L) / n_*(D_L) n_*(D_S) D_S^{2-\gamma} D_L^2 d D_S}{\int_{D_{S,min}}^{D_{S,max}} n_*(D_S) D_S^{2-\gamma} D_L^2 d D_S}. \quad (39)$$

Here D_L is derived for given $D_{8.3}$ and D_S . As illustrated in Figure 17, for the current sample we find that $\eta_{b2d} = 28\%$ if “planet” is defined by mass ratio q in the range 10^{-5} to 10^{-2} , and that $\eta_{b2d} = 35\%$ if “planet” is defined by mass in the range $1 M_{\oplus}$ to $3 M_J$. Assuming that the planet formation is no different between the bulge and the disk, these suggest that $\sim 1/3$ of all planet detections in our experiment should come from bulge events. In other words, any deviation from the above value would indicate that the bulge planet population is different from the disk planet population.

We also investigate the influence of impact parameters on the two cumulative distributions $C_q(D_{8.3})$ and $C_m(D_{8.3})$, for the purpose of better planning future similar experiments. We find that the sample of events with maximum magnifications $A_{max} > 8$, which account for 24% of all events in our sample, contributes 40%–45% of all planet sensitivities.

6. Discussion

We present the planet sensitivities of 41 microlensing events from the 2015 *Spitzer* campaign, all of which received dense coverage by OGLE-IV and KMTNet. Because of the null detection of planets in this statistical sample, we provide upper limits on the planet distribution function (Equation (35)). In particular, we find that the normalization factor $\mathcal{A} < 0.49$ at the 95% confidence level for a flat planet MF. These constraints are consistent with the previous microlensing results by Gould et al. (2010), Shvartzvald et al. (2016), and Suzuki et al. (2016).

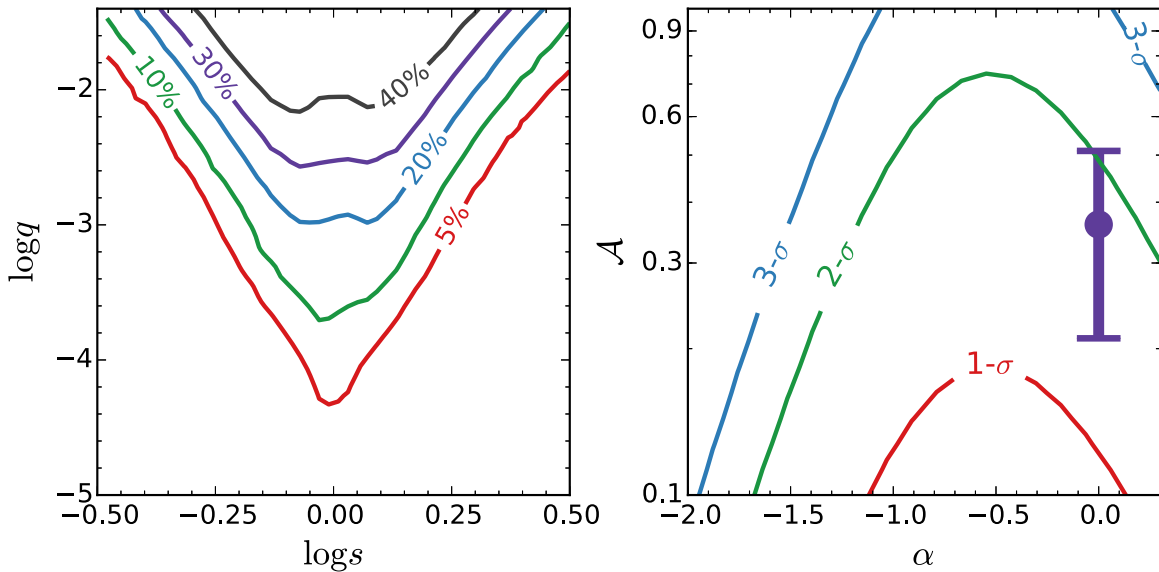


Figure 16. Left panel: planet sensitivities averaged over 41 events in our sample. Right panel: constraints on the planet distribution function based on our sample. Here α is the slope of the planet MF, and \mathcal{A} is the normalization factor. The purple point is the measurement by Gould et al. (2010), which assumed a flat ($\alpha = 0$) planet MF.

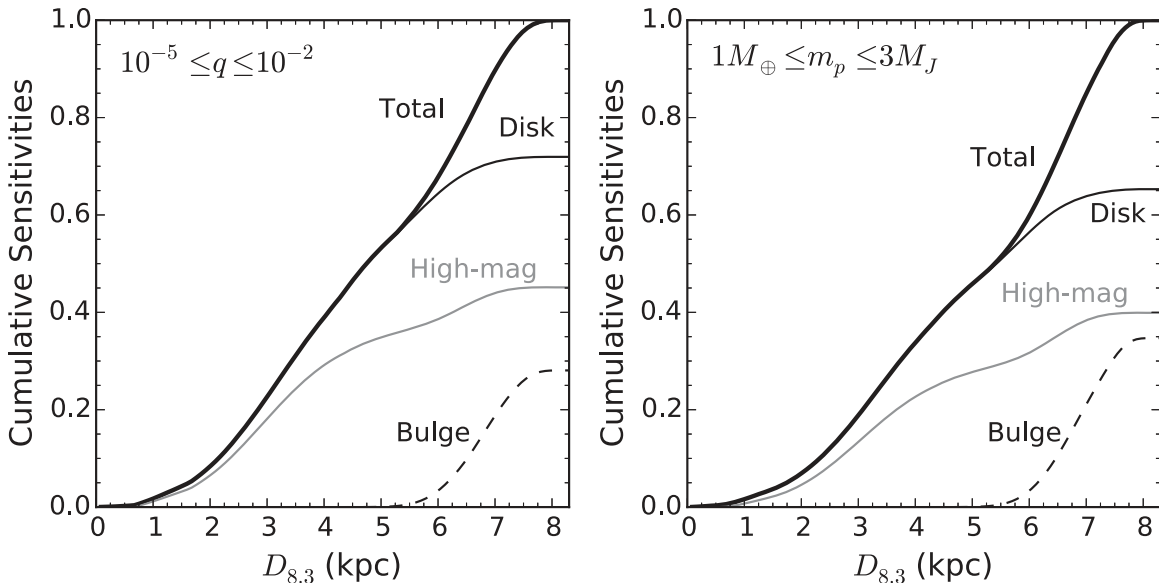


Figure 17. Normalized cumulative planet sensitivities along the lens distance parameter $D_{8.3}$. Planets are defined by $10^{-5} \leq q \leq 10^{-2}$ in the left panel and by $1 M_{\oplus} \leq m_p \leq 3 M_J$ in the right panel. Contributions from the disk events, bulge events, and relatively high magnification ($A_{\max} > 8$) events are also shown separately.

We develop the methodology to statistically study the Galactic distribution of planets using microlensing parallax measurements. In particular, we provide mathematical descriptions for estimating the lens mass M_L and distance parameter $D_{8.3}$ with the measurement of the microlensing parallax vector π_E . Although such statistical estimates cannot be used as deterministic measurements of individual microlenses, they are in general fairly compact and independent of the details of the input Galactic model, because of the kinematic information contained by π_E (Figure 2; see also Han & Gould 1995). In fact, the majority of events in our raw sample have uncertainties on the distance parameter, $\sigma(D_{8.3}) \lesssim 1$ kpc. For the purpose of determining a Galactic distribution of planets, we decide to use $\sigma(D_{8.3}) < 1.4$ kpc as the criterion for claiming a good parallax measurement. Note that this criterion is formed based

on a planet-free sample, meaning that it is not biased by the presence of any planet detection. Events that show planetary perturbations, however, do have smaller uncertainties on the lens distance parameter. This is partly because of the breakdown of the fourfold degeneracy, but mostly because most of them show the finite-source effect (Zhu et al. 2014), which, when combined with the microlensing parallax measurement, yields deterministic lens distance and mass measurements (e.g., Street et al. 2016). Therefore, while our current sample is planet-free, we suggest that the inclusion of any future planetary event in the statistical sample should be based on the $\sigma(D_{8.3})$ that is estimated in the same way as a single-lens event, rather than the $\sigma(D_{8.3})$ that is determined by combining information from the planetary anomaly (e.g., the finite-source effect).

We use one of the published planetary events from the 2015 *Spitzer* campaign, OGLE-2015-BLG-0966 (Street et al. 2016), as an example to demonstrate whether a planet can be included in the sample or not. To remove the influence of the planet, we replace those data points that are affected by the planet with pseudo-data points that are generated based on the single-lens model.²⁷ We then search for lens parameters of four degenerate solutions. The lens distance parameter $D_{8.3}$ is then estimated following the equations in Section 4.3. From this we then determine the median and the half-width of the 68% confidence interval and find $D_{8.3} = 3.1 \pm 1.2$ kpc. According to the criterion $\sigma(D_{8.3}) < 1.4$ kpc, the associated planet would be included in the statistical sample if this event had been covered by KMTNet.²⁸

We note that we developed the criterion for “measured π_E ” before looking at OGLE-2015-BLG-0966 (or any other *Spitzer* planetary event), precisely to allow us to advocate for this criterion without in any way being influenced by a subconscious desire to include more planets in the sample.

Furthermore, high-magnification events such as OGLE-2015-BLG-0966 provide additional constraints on the lens mass and distance. Even if the lens is a point mass, if the lens transits the face of the source (i.e., the source crosses the caustic of a point mass, which is a single point), the event will show the finite-source effect. In the presence of the finite-source effect, the angular Einstein radius and thus the lens mass and distance are directly measured given a measurement of the parallax (Yoo et al. 2004). Furthermore, the absence of finite-source effects provides an upper limit on the scaled source radius $\rho \lesssim u_0$, which corresponds to a lower limit on π_{rel} and an upper limit on $D_{8.3}$. In this way, this additional constraint reduces the uncertainty on the distance parameter $D_{8.3}$ and thus potentially increases the chance for high-magnification events to be included in the statistical sample. This is important because high-magnification events have much higher sensitivity to planets compared to typical events (Griest & Safizadeh 1998). It is nevertheless unbiased in terms of planet detections, since the additional information used here does not rely on the presence of planets. In the case of OGLE-2015-BLG-0966, this additional constraint yields $D_{8.3} < 6.9$ kpc and thus reduces $\sigma(D_{8.3})$ to 1.1 kpc.

Based on the current sample, we find that $\sim 1/3$ of all planet sensitivities come from events in the bulge. Assuming that the planet distribution is the same in the bulge as in the disk, this result predicts that $\sim 1/3$ of all planet detections from our experiment will be in the bulge. In the future, deviations from this prediction can then be used to constrain the abundance of planets in the bulge relative to the disk.

Work by W.Z. and A.G. was supported by NSF grant AST-1516842. Work by A.G. was also supported by JPL grant 1500811. Work by C.H. was supported by the Creative Research Initiative Program (2009-0081561) of the National Research Foundation of Korea. The OGLE project has received funding from the National Science Centre, Poland, grant MAESTRO 2014/14/A/ST9/00121 to A.U. This work is based in part on observations made with the *Spitzer Space Telescope*, which is operated by the Jet Propulsion Laboratory,

²⁷ We use the nonplanetary parameters of the planetary model as parameters for this single-lens model.

²⁸ In fact, it fell in a gap between CCD chips of the camera, which would not have occurred under the 2016 KMTNet observing strategy.

California Institute of Technology, under a contract with NASA. This research has made use of the KMTNet system operated by KASI, and the data were obtained at three host sites of CTIO in Chile, SAAO in South Africa, and SSO in Australia.

Appendix A Source Distance Bias

We parameterize the luminosity function of bulge stars in I band given by Holtzman et al. (1998) as

$$\log N = aM_I + b = \begin{cases} 0.57M_I + 0.81 & , (M_I < 3.5) \\ 0.16M_I + 2.24 & , (M_I > 3.5) \end{cases}, \quad (40)$$

where N is the number of stars per square arcmin per magnitude. In terms of the microlensing observable, I_S , which is the source apparent I magnitude at baseline, the number of stars per unit area per magnitude is then

$$N = 10^{a(I_S - A_I - 5 \log D_S + 5) + b}. \quad (41)$$

Here A_I is the extinction to the source. For given I_S and D_S , a and b can be determined by comparing the derived M_I with the magnitude threshold in Equation (40).

In principle, one should use the full expression of N given in Equation (41) as the third factor in the weight of D_S (Equations (28) and (39)). This is because the values of a and b may change as D_S varies. However, with the extinction map given in Nataf et al. (2013), we find that nearly all sources in our sample have M_I considerably below 3.5 for typical $D_S \sim 8.3$ kpc, so we use the simplified weight $D_S^{-\gamma}$ and choose $\gamma = 5 \times 0.57 = 2.85$.

We note that the resulting lens distributions are insensitive to the choice of γ . For example, the variation in the $D_{8.3}$ distribution derived by Equation (28) is limited to within 5% if $\gamma = 1$ is used, and the shift in the median of $D_{8.3}$ is $\lesssim 0.1$ kpc (see the left panel of Figure 18). This is a consequence of three factors. First, the number density term, n_S , dominates over $D_S^{2-\gamma}$, so that the mean source distance, $\langle D_S \rangle \equiv (\int n_S D_S^{3-\gamma} dD_S) / (\int n_S D_S^{2-\gamma} dD_S)$, only differs by 0.16 kpc when γ changes from 2.85 to 1. Second, we derive the lens position in terms of $D_{8.3}$ rather than the actual lens distance D_L , and $D_{8.3}$ is less dependent on D_S than D_L is. To further demonstrate this point, we also derive the distribution of D_L , which involves

$$\frac{d^4 \Gamma}{d D_L dt_E^2 d^2 \tilde{\nu}_{\text{hel}}} = 4n_L D_L^2 f_{\tilde{\nu}}(\tilde{\nu}_{\text{hel}}) \frac{d\xi(M_L)}{d \log M_L} \mu_{\text{rel}}^2. \quad (42)$$

As shown in Figure 18, different choices of γ can lead D_L to differ by ~ 0.1 kpc for $D_L \gtrsim 2$ kpc, but the difference in $D_{8.3}$ is in general much smaller and only reaches ~ 0.1 kpc when $D_{8.3} \sim 4$ kpc.

The third reason is that, although the solution based on π_E measurement is fairly compact, the dispersion is still considerably large compared to ~ 0.1 kpc. As an extreme example, if the lens distribution for a fixed source distance, $\mathcal{P}(D_{8.3}|D_S)$ (or $\mathcal{P}(D_L|D_S)$), is perfectly uniform, γ will have no impact on the result at all, because terms containing γ in Equation (28) cancel out.

This argument also implies that γ has an even smaller effect for the Bayesian estimates of lens distances based on θ_E measurements, which in general have broader distributions. To prove this point, we first provide the corresponding $\mathcal{P}(D_L|D_S)$

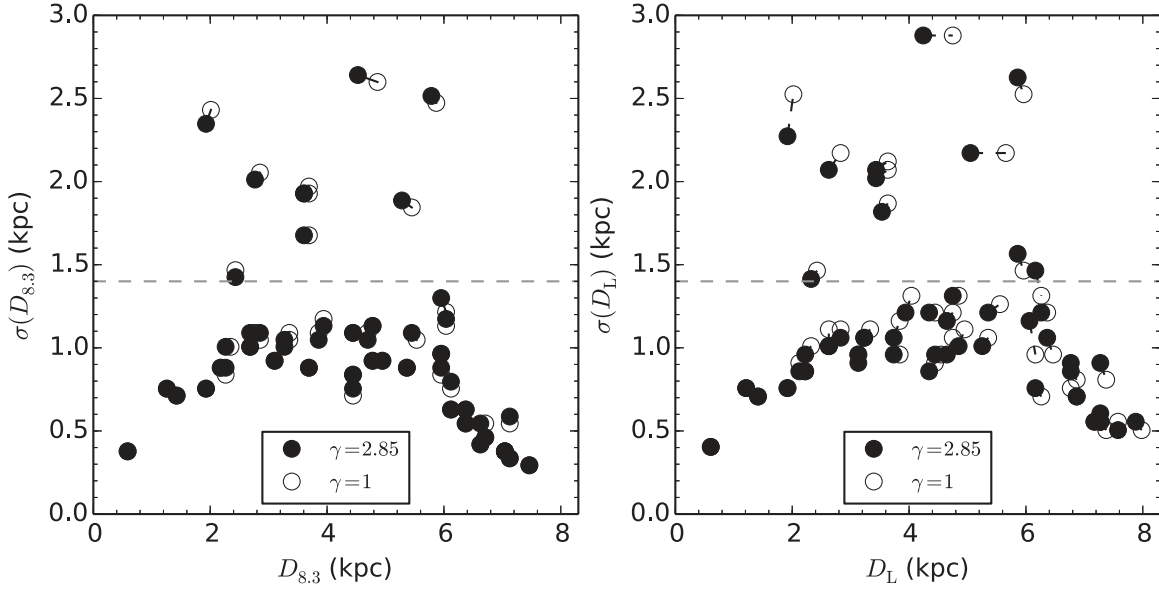


Figure 18. Impact of γ in median and dispersion of the lens distance parameter $D_{8.3}$ (left panel) and D_L for the 50 events in the raw sample. The gray dashed line is the threshold for claiming a “good” parallax measurement. See Figure 7 for more details.

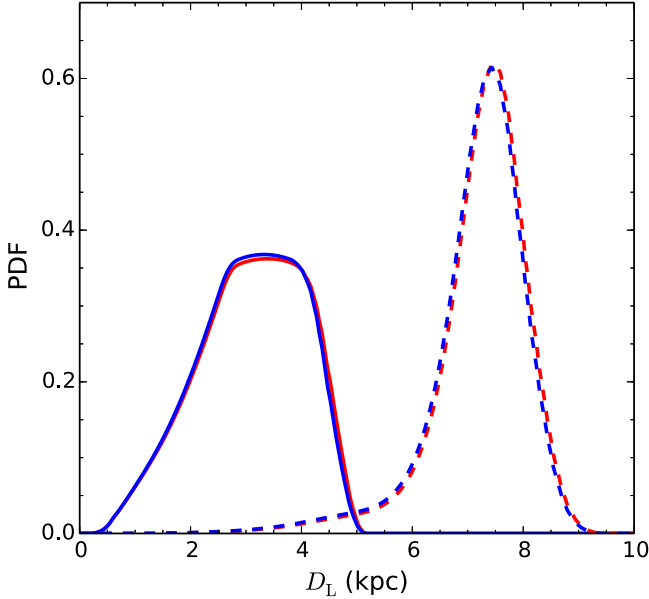


Figure 19. Lens distance distributions of OGLE-2005-BLG-169 (solid curves) and MOA-2011-BLG-293 (dashed curves) based on θ_E measurements. Results with $\gamma = 1$ are shown in red, and those with $\gamma = 2.85$ are shown in blue. The difference in the median of D_L is less than 0.05 kpc. In the derivation, a Kroupa-like MF (Equation (18)) has been assumed. We also assume perfect knowledge of θ_E and t_E , meaning that $P(\theta_E|\text{Data})$ and $P(t_E|\text{Data})$ in Equation (43) are both Dirac- δ functions.

in the case that θ_E rather than π_E is measured,²⁹

$$\mathcal{P}(D_L|D_S) = \int \frac{d^3\Gamma}{dD_L d\theta_E dt_E} P(\theta_E|\text{Data}) P(t_E|\text{Data}) d\theta_E dt_E;$$

$$\frac{d^3\Gamma}{dD_L d\theta_E dt_E} = 4n_L D_L^2 f_\mu(\mu_{\text{rel}}) \frac{d\xi(M_L)}{d \log M_L} \frac{\mu_{\text{rel}}^2}{t_E}.$$
(43)

²⁹ Note that now the correction from t_E to t'_E is no longer achievable. We therefore assume $t'_E = t_E$, which is in general a reasonable assumption (since $v_\oplus \ll \bar{v}_{\text{hel}}$).

Here $f_\mu(\mu_{\text{rel}})$ is the probability distribution of μ_{rel} and is given by

$$f_\mu(\mu_{\text{rel}}) = \frac{\mu_{\text{rel}}}{2\pi\sigma_l\sigma_b} \int_0^{2\pi} \exp\left[-\frac{(\mu_{\text{rel}} \cos\theta - \bar{\mu}_{\text{rel}}^l)^2}{2\sigma_l^2} - \frac{(\mu_{\text{rel}} \sin\theta - \bar{\mu}_{\text{rel}}^b)^2}{2\sigma_b^2}\right] d\theta,$$
(44)

where $\bar{\mu}_{\text{rel}}^l$ and σ_l are the mean and dispersion of μ_{rel} along the l direction and $\bar{\mu}_{\text{rel}}^b$ and σ_b are the counterparts along the b direction, respectively. With these formulae, we then derive the lens distances of two published events, OGLE-2005-BLG-169 (a typical disk event; Gould et al. 2006; Batista et al. 2015; Bennett et al. 2015) and MOA-2011-BLG-293 (a typical bulge event; Yee et al. 2012; Batista et al. 2014), and show the resulting distributions in Figure 19. As expected, the differences in D_L arising from different values of γ are smaller compared to cases with π_E measurements.

Appendix B Integral of Gaussian Product

The estimates of lens mass M_L and distance parameter $D_{8.3}$ (Equation (28)) involve the integral of the product of two multidimensional Gaussian probability functions. Although this result has probably been well known for centuries, we provide an explicit representation below simply for completeness.

The integral of the product of two multidimensional Gaussian distributions can be written as

$$P(\mathbf{x}) = \int \mathcal{N}(\mathbf{x}|\boldsymbol{\mu}_1, \mathbb{C}_1) \mathcal{N}(\mathbf{x}|\boldsymbol{\mu}_2, \mathbb{C}_2) d^n \mathbf{x}.$$
(45)

Here $\mathcal{N}(\mathbf{x}|\boldsymbol{\mu}, \mathbb{C})$ is the notation for a multidimensional Gaussian probability function with mean $\boldsymbol{\mu}$ and covariance

matrix \mathbb{C} ,

$$\mathcal{N}(\mathbf{x}|\boldsymbol{\mu}, \mathbb{C}) \equiv \frac{\exp\left[-\frac{1}{2}(\mathbf{x} - \boldsymbol{\mu})^T \mathbb{C}^{-1}(\mathbf{x} - \boldsymbol{\mu})\right]}{\sqrt{|2\pi\mathbb{C}|}}. \quad (46)$$

The integral given by Equation (45) can be computed analytically by “completing the squares,”

$$P(\mathbf{x}) = \sqrt{\frac{|2\pi\hat{\mathbb{C}}|}{|2\pi\mathbb{C}_1||2\pi\mathbb{C}_2|}} \times \exp\left[-\frac{1}{2}(\boldsymbol{\mu}_1^T \mathbb{C}_1^{-1} \boldsymbol{\mu}_1 + \boldsymbol{\mu}_2^T \mathbb{C}_2^{-1} \boldsymbol{\mu}_2 - \hat{\boldsymbol{\mu}}^T \hat{\mathbb{C}}^{-1} \hat{\boldsymbol{\mu}})\right], \quad (47)$$

where

$$\hat{\mathbb{C}}^{-1} \equiv \mathbb{C}_1^{-1} + \mathbb{C}_2^{-1}; \quad \hat{\boldsymbol{\mu}} \equiv \hat{\mathbb{C}}(\mathbb{C}_1^{-1} \boldsymbol{\mu}_1 + \mathbb{C}_2^{-1} \boldsymbol{\mu}_2). \quad (48)$$

ORCID iDs

Wei Zhu (祝伟)  <https://orcid.org/0000-0003-4027-4711>
 S. Calchi Novati  <https://orcid.org/0000-0002-7669-1069>
 S.-J. Chung  <https://orcid.org/0000-0001-6285-4528>
 Y. K. Jung  <https://orcid.org/0000-0002-0314-6000>
 Y.-H. Ryu  <https://orcid.org/0000-0001-9823-2907>
 M. D. Albrow  <https://orcid.org/0000-0003-3316-4012>
 J. C. Yee  <https://orcid.org/0000-0001-9481-7123>
 C. Han  <https://orcid.org/0000-0002-2641-9964>
 K.-H. Hwang  <https://orcid.org/0000-0002-9241-4117>
 D.-J. Kim  <https://orcid.org/0000-0002-7038-2118>
 R. W. Pogge  <https://orcid.org/0000-0003-1435-3053>
 P. Pietrukowicz  <https://orcid.org/0000-0002-2339-5899>
 J. Skowron  <https://orcid.org/0000-0002-2335-1730>
 S. Kozłowski  <https://orcid.org/0000-0003-4084-880X>
 S. Carey  <https://orcid.org/0000-0002-0221-6871>
 B. S. Gaudi  <https://orcid.org/0000-0003-0395-9869>
 C. B. Henderson  <https://orcid.org/0000-0001-8877-9060>
 Y. Shvartzvald  <https://orcid.org/0000-0003-1525-5041>

References

Alard, C., & Lupton, R. H. 1998, *ApJ*, 503, 325
 Albrow, M. D., Home, K., Bramich, D. M., et al. 2009, *MNRAS*, 397, 2099
 Bahcall, J. N. 1986, *ARA&A*, 24, 577
 Batista, V., Beaulieu, J.-P., Bennett, D. P., et al. 2015, *ApJ*, 808, 170
 Batista, V., Beaulieu, J.-P., Gould, A., et al. 2014, *ApJ*, 780, 54
 Bennett, D. P., Bhattacharya, A., Anderson, J., et al. 2015, *ApJ*, 808, 169
 Bond, I. A., Abe, F., Dodd, R. J., et al. 2001, *MNRAS*, 327, 868
 Bozza, V., Shvartzvald, Y., Udalski, A., et al. 2016, *ApJ*, 820, 79
 Burke, C. J., Christiansen, J. L., Mullally, F., et al. 2015, *ApJ*, 809, 8
 Calchi Novati, S., Gould, A., Udalski, A., et al. 2015, *ApJ*, 804, 20
 Calchi Novati, S., Gould, A., Yee, J. C., et al. 2015, *ApJ*, 814, 92
 Calchi Novati, S., & Scarpetta, G. 2016, *ApJ*, 824, 109
 Cao, L., Mao, S., Nataf, D., Rattenbury, N. J., & Gould, A. 2013, *MNRAS*, 434, 595
 Chen, B., Stoughton, C., Smith, J. A., et al. 2001, *ApJ*, 553, 184
 Chung, S.-J., Zhu, W., Udalski, A., et al. 2017, *ApJ*, 838, 154
 Clanton, C., & Gaudi, B. S. 2016, *ApJ*, 819, 125
 DePoy, D. L., Atwood, B., Belville, S. R., et al. 2003, *Proc. SPIE*, 4841, 827
 Dong, S., Udalski, A., Gould, A., et al. 2007, *ApJ*, 664, 862
 Dong, S., & Zhu, Z. 2013, *ApJ*, 778, 53
 Dwek, E., Arendt, R. G., Hauser, M. G., et al. 1995, *ApJ*, 445, 716

Eggenberger, A., Udry, S., Chauvin, G., et al. 2007, *A&A*, 474, 273
 Fischer, D. A., & Valenti, J. 2005, *ApJ*, 622, 1102
 Foreman-Mackey, D., Hogg, D. W., Lang, D., & Goodman, J. 2013, *PASP*, 125, 306
 Fressin, F., Torres, G., Charbonneau, D., et al. 2013, *ApJ*, 766, 81
 Gaudi, B. S., Albrow, M. D., An, J., et al. 2002, *ApJ*, 566, 463
 Gaudi, B. S., & Gould, A. 1997a, *ApJ*, 477, 152
 Gaudi, B. S., & Gould, A. 1997b, *ApJ*, 486, 85
 Gaudi, B. S., & Sackett, P. D. 2000, *ApJ*, 528, 56
 Gillessen, S., Eisenhauer, F., Trippe, S., et al. 2009, *ApJ*, 692, 1075
 Gould, A. 1992, *ApJ*, 392, 442
 Gould, A. 1994, *ApJL*, 421, L75
 Gould, A. 1995, *ApJL*, 441, L21
 Gould, A. 2004, *ApJL*, 606, 319
 Gould, A., Carey, S., & Yee, J. 2013, Spitzer Proposal ID #10036
 Gould, A., Carey, S., & Yee, J. 2014, Spitzer Proposal ID #11006
 Gould, A., Carey, S., & Yee, J. 2016, Spitzer Proposal ID #13005
 Gould, A., Dong, S., Gaudi, B. S., et al. 2010, *ApJ*, 720, 1073
 Gould, A., & Loeb, A. 1992, *ApJ*, 396, 104
 Gould, A., Udalski, A., An, D., et al. 2006, *ApJL*, 644, L37
 Gould, A., Yee, J., & Carey, S. 2015a, Spitzer Proposal ID #12013
 Gould, A., Yee, J., & Carey, S. 2015b, Spitzer Proposal ID #12015
 Graff, D. S., & Gould, A. 2002, *ApJ*, 580, 253
 Griest, K., & Safizadeh, N. 1998, *ApJ*, 500, 37
 Han, C. 2006, *ApJ*, 638, 1080
 Han, C., & Gould, A. 1995, *ApJ*, 447, 53
 Han, C., Udalski, A., Gould, A., et al. 2017, *ApJ*, 834, 82
 Holtzman, J. A., Watson, A. M., Baum, W. A., et al. 1998, *AJ*, 115, 1946
 Johnson, J. A., Aller, K. M., Howard, A. W., & Crepp, J. R. 2010, *PASP*, 122, 905
 Kent, S. M., Dame, T. M., & Fazio, G. 1991, *ApJ*, 378, 131
 Kim, S.-L., Lee, C.-U., Park, B.-G., et al. 2016, *JKAS*, 49, 37
 Kiraga, M., & Paczynski, B. 1994, *ApJL*, 430, L101
 Kroupa, P. 2001, *MNRAS*, 322, 231
 Mao, S., & Paczynski, B. 1991, *ApJL*, 374, L37
 Nataf, D. M., Gould, A., Fouqué, P., et al. 2013, *ApJ*, 769, 88
 Penny, M. T., Henderson, C. B., & Clanton, C. 2016, *ApJ*, 830, 150
 Petigura, E. A., Howard, A. W., & Marcy, G. W. 2013, *PNAS*, 110, 19273
 Poleski, R., Udalski, A., Gould, A., et al. 2013, *ApJ*, 776, 76
 Poleski, R., Zhu, W., Christie, G. W., et al. 2016, *ApJ*, 823, 63
 Refsdal, S. 1966, *MNRAS*, 134, 315
 Reid, M. J., & Brunthaler, A. 2004, *ApJ*, 616, 872
 Reid, M. J., Menten, K. M., Brunthaler, A., et al. 2014, *ApJ*, 783, 130
 Rhie, S. H., Bennett, D. P., Becker, A. C., et al. 2000, *ApJ*, 533, 378
 Robin, A. C., Reylé, C., Derrière, S., & Picaud, S. 2003, *A&A*, 409, 523
 Sako, T., Sekiguchi, T., Sasaki, M., et al. 2008, *ExA*, 22, 51
 Santos, N. C., Israelian, G., & Mayor, M. 2001, *A&A*, 373, 1019
 Santos, N. C., Israelian, G., Mayor, M., Rebolo, R., & Udry, S. 2003, *A&A*, 398, 363
 Schechter, P. L., Mateo, M., & Saha, A. 1993, *PASP*, 105, 1342
 Schönrich, R., Binney, J., & Dehnen, W. 2010, *MNRAS*, 403, 1829
 Shvartzvald, Y., Mao, S., Udalski, A., et al. 2016, *MNRAS*, 457, 4089
 Smith, M. C., Mao, S., & Paczyński, B. 2003, *MNRAS*, 339, 925
 Street, R. A., Udalski, A., Calchi Novati, S., et al. 2016, *ApJ*, 819, 93
 Suzuki, D., Bennett, D. P., Sumi, T., et al. 2016, *ApJ*, 833, 145
 Thompson, T. A. 2013, *MNRAS*, 431, 63
 Udalski, A. 2003, *AcA*, 53, 291
 Udalski, A., Szymanski, M., Kaluzny, J., et al. 1994, *AcA*, 44, 317
 Udalski, A., Szymański, M. K., & Szymański, G. 2015a *AcA*, 65, 1
 Udalski, A., Yee, J. C., Gould, A., et al. 2015b, *ApJ*, 799, 237
 Wang, J., & Fischer, D. A. 2015, *AJ*, 149, 14
 Wang, J., Xie, J.-W., Barclay, T., & Fischer, D. A. 2014, *ApJ*, 783, 4
 Wegg, C., & Gerhard, O. 2013, *MNRAS*, 435, 1874
 Wozniak, P. R. 2000, *AcA*, 50, 421
 Wyrzykowski, Ł., Rynkiewicz, A. E., Skowron, J., et al. 2015, *ApJS*, 216, 12
 Yee, J. C., Gould, A., & Beichman, C., 2015, *ApJ*, 810, 155
 Yee, J. C., Shvartzvald, Y., Gal-Yam, A., et al. 2012, *ApJ*, 755, 102
 Yee, J. C., Udalski, A., Calchi Novati, S., et al. 2015, *ApJ*, 802, 76
 Yoo, J., DePoy, D. L., Gal-Yam, A., et al. 2004, *ApJ*, 603, 139
 Zhu, W., Calchi Novati, S., Gould, A., et al. 2016, *ApJ*, 825, 60
 Zhu, W., Gould, A., Beichman, C., et al. 2015, *ApJ*, 814, 129
 Zhu, W., Penny, M., Mao, S., Gould, A., & Gendron, R. 2014, *ApJ*, 788, 73
 Zhu, W., Udalski, A., Gould, A., et al. 2015, *ApJ*, 805, 8
 Zhu, W., Wang, J., & Huang, C. 2016, *ApJ*, 832, 196